ISTANBUL TECHNICAL UNIVERSITY ★ GRADUATE SCHOOL OF SCIENCE ENGINEERING AND TECHNOLOGY

A NUMERICAL STUDY ON THE INTERACTION OF FLOW AND COMBUSTION IN SOLID PROPELLANT ROCKET MOTORS

Ph.D. THESIS

Mehmet Özer HAVLUCU

Department of Mechanical Engineering

Mechanical Engineering Programme

DECEMBER 2017

ISTANBUL TECHNICAL UNIVERSITY ★ GRADUATE SCHOOL OF SCIENCE ENGINEERING AND TECHNOLOGY

A NUMERICAL STUDY ON THE INTERACTION OF FLOW AND COMBUSTION IN SOLID PROPELLANT ROCKET MOTORS

Ph.D. THESIS

Mehmet Özer HAVLUCU
(503052015)

Department of Mechanical Engineering

Mechanical Engineering Programme

Thesis Advisor: Prof. Dr. Kadir KIRKKÖPRÜ

DECEMBER 2017

İSTANBUL TEKNİK ÜNİVERSİTESİ ★ FEN BİLİMLERİ ENSTİTÜSÜ

KATI YAKITLI ROKET MOTORLARINDA AKIŞ YANMA ETKİLEŞİMİ ÜZERİNE SAYISAL BİR ÇALIŞMA

DOKTORA TEZİ

Mehmet Özer HAVLUCU
(503052015)

Makina Mühendisliği Anabilim Dalı

Makina Mühendisliği Programı

Tez Danışmanı: Prof. Dr. Kadir KIRKKÖPRÜ

ARALIK 2017

Mehmet Özer HAVLUCU,a Ph.D. student of İTU Graduate School of Science Engineering and Technology student ID 503052015, successfully defended the thesis/dissertation entitled “A NUMERICAL STUDY ON THE INTERACTION OF FLOW AND COMBUSTION IN SOLID PROPELLANT ROCKET MOTORS”, which he prepared after fulfilling the requirements specified in the associated legislations, before the jury whose signatures are below.

Thesis Advisor :	**Prof. Dr. Kadir KIRKKÖPRÜ** Istanbul Technical University	.....
Jury Members :	**Prof. Dr. Erkan AYDER** Istanbul Technical University	.....
	Prof. Dr. Fırat Oğuz EDİS Istanbul Technical University	.....
	Asst. Prof. Dr. Levent Ali KAVURMACIOĞLU Istanbul Technical University	.....
	Assoc. Prof. Dr. Emre ALPMAN Marmara University	.....

Date of Submission : 07 November 2017
Date of Defense : 25 December 2017

To my dad,

FOREWORD

I want to say how thankful I am for all the help and support of the people during my entire study. It is a great pleasure to thank my advisor Prof. Dr. Kadir KIRKKÖPRÜ, who provided me assistance, encouragement and guidance and especially incisive suggestions throughout this whole research.

I would like to use the opportunity to thank my friend Cem DOLU, with whom I had many discussions during the study and he gave me useful ideas.

I wish to extend my sincere thanks for my beloved wife Dr. Gül Nilay İNOĞLU HAVLUCU for her patience and advices over the whole Ph.D. period. Thanks for my lovely little son Derin Demir HAVLUCU, who brought luck to me. I don't want to forget my whole family including my mother and my two sisters for their support.

In addition, special thanks to my uncle M.Sc. Mechanical Engineer Mehmet Tevfik İNAN, who gave me fascinating assistance throughout the study and my life.

November 2017

Mehmet Özer HAVLUCU
M.Sc. Mechanical Engineer

TABLE OF CONTENTS

Page

FOREWORD ..... **ix**
TABLE OF CONTENTS ..... **xi**
ABBREVIATIONS ..... **xiii**
SYMBOLS ..... **xv**
LIST OF FIGURES ..... **xvii**
SUMMARY ..... **xxi**
ÖZET ..... **xxiii**
1. INTRODUCTION **1**
2. MATHEMATICAL MODEL **5**
2.1 Governing Equations 5
2.2 Chemical Rate Expressions 9
3. NUMERICAL MODEL **13**
3.1 Solution Method 13
3.2 Stiffness Problem 14
3.3 Regressive Boundary Model 15
4. INITIAL AND BOUNDARY CONDITIONS **19**
4.1 Inflow Boundary Conditions 19
4.2 Adiabatic Solid Wall Boundary Condition 20
4.3 Symmetry Boundary Condition 20
4.4 Outflow Boundary Condition 20
5. RESULTS AND DISCUSSION **21**
5.1 Cold Flow Validation 21
5.1.1 Onerac 1 with non-regressive boundary 21
5.1.2 Onerac 1 with regressive boundary 24
5.2 Reacting Flow Validation 25
5.2.1 Flow in a duct with side-wall mass injection 25
5.2.2 Flow in a duct with end-burning mass injection 28
5.3 Reacting Flow with Regressive Boundary Computations 33
5.3.1 Constant rate regressive boundary model for lab-scale motor 33
5.3.1.1 Thrust curves 38
5.3.2 Pressure dependent regressive boundary model computations 43
5.3.2.1 Pressure dependent regressive rate model for lab-scale motor 43
5.3.2.2 Pressure dependent regressive rate model for Onerac 1 motor 52
6. CONCLUSIONS **59**
REFERENCES **63**
APPENDICES **69**
APPENDIX A 70
APPENDIX B 71
APPENDIX C 72
CURRICULUM VITAE **73**

ABBREVIATIONS

KTF	**:** Kullanıcı Tanımlı Fonksiyon
KYRM	**:** Katı Yakıtlı Roket Motoru
kPa	**:** Kilopascal
MPa	**:** Megapascal
SRM	**:** Solid Rocket Motor
UDF	**:** User Defined Function

SYMBOLS

$\boldsymbol{A_r}$	**:** Pre-exponential factor
$\boldsymbol{A_e}$	**:** Cross sectional area at the exit of the nozzle
$\boldsymbol{C_{i,r}}$	**:** Molar concentration of species *i* in reaction *r*
$\boldsymbol{C_p}$	**:** Specific heat of the mixture
$\boldsymbol{C_{p,i}}$	**:** Specific heat of each species
$\boldsymbol{D_i}$	**:** Diffusion coefficient of each species
$\boldsymbol{D_{i,j}}$	**:** Binary diffusion coefficient of component *i* in component *j*
$\boldsymbol{D_{i,m}}$	**:** Diffusion coefficient of each speciesin the mixture
$\boldsymbol{E}$	**:** Total energy
$\boldsymbol{E_a}$	**:** Activation energy
$\boldsymbol{h}$	**:** Internal enthalpy
$\boldsymbol{h_i}$	**:** Internal enthalpy of each species
$\boldsymbol{H}$	**:** Total enthalpy
$\boldsymbol{k_{f,r}}$	**:** Forward rate constant
$\boldsymbol{N}$	**:** Number of species
$\boldsymbol{n}$	**:** Pressure index or pressure exponent
$\boldsymbol{\dot{m}}$	**:** Mass flow rate
$\boldsymbol{M_{w,i}}$	**:** Molecular weight of each species
$\boldsymbol{p}$	**:** Pressure
$\boldsymbol{p_e}$	**:** Exhaust gas pressure
$\boldsymbol{p_0}$	**:** Ambient pressure
$\boldsymbol{\dot{r}_b}$	**:** Burning rate of the boundary
$\boldsymbol{R}$	**:** Universal gas constant
$\boldsymbol{R_i}$	**:** Volumetric rate of creation of each species
$\boldsymbol{\widehat{R}_{i,r}}$	**:** Arrhenius molar rate of creation or destruction of each species *i* in each reaction *r*
q	**:** Heat of chemical reaction
s	**:** Source term of each species
$\boldsymbol{s_h}$	**:** Heat of reaction for each species
$\boldsymbol{s_N}$	**:** Source term
$\boldsymbol{t}$	**:** Time
$\boldsymbol{T}$	**:** Temperature
$\boldsymbol{T_{inj}}$	**:** Injection temperature
$\boldsymbol{T_{ref}}$	**:** Reference temperature
$\boldsymbol{u}$	**:** Velocity in x direction
$\boldsymbol{v}$	**:** Velocity in y direction
$\boldsymbol{V_e}$	**:** Exit velocity of the gaseous mixture from the nozzle
$\boldsymbol{V_g}$	**:** Velocity of gas leaving the solid propellant
$\boldsymbol{V_{inj}}$	**:** Injection velocity
$\boldsymbol{x_{new}}$	**:** Calculated new x-coordinate

$\boldsymbol{x_{old}}$	**:** x-coordinate of the boundary in the previous time step
$\boldsymbol{X_i}$	**:** Mole fraction of each species
$\boldsymbol{Y_i}$	**:** Mass fraction of each species
$\boldsymbol{\alpha}$	**:** Burn rate coefficient
$\boldsymbol{a_{k,i}}$	**:** Polynomial coefficient for specific heat calculation of species *i*
$\boldsymbol{\beta_r}$	**:** Temperature exponent
$\Delta\boldsymbol{t}$	**:** Time step
$\boldsymbol{\rho}$	**:** Density of the gaseous mixture
$\boldsymbol{\rho_i}$	**:** Density of each species
$\boldsymbol{\rho_g}$	**:** Density of gas leaving the solid propellant
$\boldsymbol{\rho_p}$	**:** Density of solid propellant
$\boldsymbol{\vartheta'_{i,r}}$	**:** Stoichiometric coefficients for the reactants
$\boldsymbol{\vartheta''_{i,r}}$	**:** Stoichiometric coefficients for the products
$\boldsymbol{\eta_{i,r}}$	**:** Rate exponent for species *i* in reaction *r*

LIST OF FIGURES

Page

Figure 3.1 : Grid structure next to the end-burning boundary in the lab scale motor. **14**
Figure 3.2 : Surface regression model **16**
Figure 5.1 : Geometry of Onerac 1 . ..... **21**
Figure 5.2 : Computational domain of Onerac 1 with boundary conditions **22**
Figure 5.3 : Comparison of pressure contours (bar) a) Work of Vuillot b) Work of Uygun c) Current study. **22**
Figure 5.4 : Comparison of Mach number contours a) Work of Vuillot b) Work of Uygun c) Current study. **23**
Figure 5.5 : Contours of streamlines a) Work of Uygun b) Current study. **23**
Figure 5.6 : Time history of head end pressure a) Present work b) Work of Uygun. **24**
Figure 5.7 : Streamlines comparison during the propellant regression a) Present work b) Work of Uygun. **24**
Figure 5.8 : Time history for head-end pressure a) Current work b) Work of Uygun **25**
Figure 5.9 : Geometric representation of the side wall mass injection **26**
Figure 5.10 : Non-uniform grid extending from the mass injecting wall to the symmetry line **26**
Figure 5.11 : Comparison of Mach number contours a) Study of Yang b) Current study. **27**
Figure 5.12 : Comparison of pressure contours (Pa) a) Study of Yang b) Current study. **27**
Figure 5.13 : Comparison of temperature and heat release variations a) Study of Yang b) Current study. **28**
Figure 5.14 : Geometric representation of the lab-scale motor..... **29**
Figure 5.15 : Temperature and mass fractions along x-axis from the burning end. . **31**
Figure 5.16 : Comparison of temperature contours a) Contour map from the work of Yumusak b) Contour map from the current study. **32**
Figure 5.17 : Comparison of Mach number contours a) Contour map from the work of Yumusak b) Contour map from the current study. **32**
Figure 5.18 : Geometric representation of the lab-scale motor with attached solid fuel. **33**
Figure 5.19 : Temperature profiles from the burning end with regression to x=1 mm corresponding t= 143ms and with no regression and for inlet temperature of 350 K. **35**
Figure 5.20 : Temperature profiles from the burning end with regression to x=1 mm corresponding t= 143ms and with no regression for minimum grid size of 0.03 mm, 0.015 mm and 0.0075 mm and for inlet temperature of 350 K. **36**

Figure 5.21 : Temperature profiles from the burning end with regression to x=1 mm corresponding t= 143ms and with no regression and for inlet temperature of 800 K. **36**
Figure 5.22 : Temperature profiles from the burning end with regression to x=1 mm corresponding t= 143ms and for inlet temperatures of 350 K and 800 K. **37**
Figure 5.23 : Temperature profiles from the burning end with regression to x=1 mm corresponding t= 143ms for H_2 and C_3H_8 combustion. **37**
Figure 5.24 : Velocity of gas mixture versus distance from the burning end with regression to x=1 mm corresponding t=143ms and with no regression and for inlet temperature of 350 K. **38**
Figure 5.25 : Thrust profiles for H_2 combustion for various inlet temperatures. **40**
Figure 5.26 : Thrust profiles for C_3H_8 combustion for various inlet temperatures... **41**
Figure 5.27 : Thrust profiles for H_2 and C_3H_8 combustion, inlet temperature of 350 K for mass flux of 11.39 kg/m^{2}s. **41**
Figure 5.28 : Thrust profiles for H_2 and C_3H_8 combustion, inlet temperature of 800 K for mass flux of 11.39 kg/m^{2}s. **42**
Figure 5.29 : Comparison of burning rates for n values of 0.2, 0.4 and 0.6, where α=0.01 and for constant burning rate. **45**
Figure 5.30 : Variation of chamber pressure with time for n values of 0.2, 0.4 and 0.6, where α=0.01 and for constant burning rate. **46**
Figure 5.31 : Spatial Variations of temperature and mass fractions along x-axis from the burning end with pressure dependent burning rate when all the solid fuel is consumed at t=14 s., when n=0.6 and α=0.01 ..... **47**
Figure 5.32 : Temperature profiles from the burning end at the time when all the solid fuel is consumed with constant burning rate at t=14.35 s and pressure dependent burning rate at t=14 s, n=0.6 and α=0.01 for minimum grid sizes of 0.03 mm, 0.015 mm and 0.0075 mm when inlet temperature is 350 K. **47**
Figure 5.33 : Temperature profiles from the burning end when all the solid fuel is consumed with constant burning rate at t=14.35 s and pressure dependent burning rate at t=14 s when n=0.6 and α=0.01 for inlet temperature of 350 K. **48**
Figure 5.34 : Temperature profiles from the burning end with pressure dependent burning rate when all the solid fuel is consumed corresponding t=14 s and n=0.6, α=0.01 for inlet temperatures of 350 K and 800 K. **49**
Figure 5.35 : Temperature profiles from the burning end with pressure dependent burning rate when all the solid fuel is consumed at t=14 s, n=0.6 and α=0.01 for H_2 and C_3H_8 combustion. **50**
Figure 5.36 : Axial variation of velocity of gas mixture from the burning end when all the solid fuel is consumed at t=14.35 s for constant burning rate and t=14 s, n=0.6 and α=0.01 for pressure dependent burning rate for inlet temperature of 350 K. **51**
Figure 5.37 : Density variation of gas mixture with distance from the burning end when all the solid fuel is consumed at t=14.35 s for constant burning rate and t=14 s, n=0.6 and α=0.01 for pressure dependent burning rate for inlet temperature of 350 K. **51**
Figure 5.38 : Grid structure from to the burning boundary for Onerac 1. ..... **52**
Figure 5.39 : Variation of chamber pressure for n values of 0.2, 0.4 and 0.6, for α=0.01 and constant burning rate. **53**

Figure 5.40 : Comparison of burning rates for n values of 0.2, 0.4 and 0.6, when α=0.01 and constant burning rate. **54**
Figure 5.41 : Y-Velocity variation from the burning surface when all the solid fuel is consumed at t=2.52 s. when n=0.6 and α=0.01 for inlet temperature of 350 K. **55**
Figure 5.42 : X-Velocity variations from the burning surface at the locations of x=66 mm, 133 mm and 200 mm when all the solid fuel is consumed at t=2.52 s. when n=0.6 and α=0.01 for inlet temperature of 350 K. **56**
Figure 5.43 : Velocity magnitude from the burning surface at the locations of x=66 mm, 133 mm and 200 mm when all the solid fuel is consumed at t=2.52 s. when n=0.6 and α=0.01 for inlet temperature of 350 K. **56**
Figure 5.44 : Spatial variations of temperature and mass fractions along y-axis from the burning surface at x= 66 mm from the head end when all the solid fuel is consumed at t=2.52 s. when n=0.6 and α=0.01 for inlet temperature of 350 K. The centerline is 0.045 m away from the burning surface. **57**
Figure 5.45 : Temperature profiles from the burning end at the time when all the solid fuel is consumed when all the solid fuel is consumed at t=2.52 s for minimum grid lengths of 0.01 mm, 0.02 mm and 0.03 mm. Here, n=0.6 and α=0.01 for inlet temperature of 350 K. **58**

A NUMERICAL STUDY ON THE INTERACTION OF FLOW AND COMBUSTION IN SOLID PROPELLANT ROCKET MOTORS

SUMMARY

A computational model is developed for the simulation of reactive fluid flow in a solid rocket motor (SRM) chamber involving variable internal geometry associated with pressure dependent propellant burning surface regression. Complete conservation equations of mass, momentum, energy and species with finite rate chemistry are solved. Spatial discretization is obtained using second order upwind differencing scheme and temporal discretization is achieved using first order implicit method. Stiff chemistry solver is used to avoid the stiffness problem due to the high temperature gradient as well as species mass fraction gradients. Cells are highly clustered in the neighborhood of the burning part of the motor to better capture these rapid variations of flow properties within the flame zone. The computational model is capable to represent the flow with wide range of Mach number, from subsonic inlet on the burning boundary to supersonic outlet at the exit of the nozzle. The pressure and time dependent dynamic boundary is established on the burning regressive boundary. To do this, User Defined Functions (UDF's) are developed and used by means of C++ which are implemented in ANSYS Fluent 15.0. The regressive boundary, which increases the volume of the combustion chamber in time, is treated by use of remeshing techniques.

Time dependent cold and reactive flows were simulated successfully. Cold flow both with non-regressive and regressive boundary model results agreed with the numerical solutions in the literature. Reacting flow with stagnant wall simulation showed good agreement when compared with two different geometry models available in the literature. These results indicate that, the current simulation are accurately developed. Hydrogen and propane combustion processes and thrust variations in time are examined for the constant rate boundary regression. Temperature and species mass fraction variations are obtained within the flame zone. Time dependent pressure and burning rate changes are illustrated for pressure dependent burning rate calculations. Temperature, velocity and density distributions are compared for both constant burning rate and pressure dependent burning rate simulations for different geometries. The developed model can simulate reactive fluid flow in a solid rocket motor (SRM) chamber with variable internal geometry due to the pressure dependent propellant burning surface regression successfully.

KATI YAKITLI ROKET MOTORLARINDA AKIŞ YANMA ETKİLEŞİMİ ÜZERİNE SAYISAL BİR ÇALIŞMA

ÖZET

20. yüzyılın ortalarından itibaren uzaya yolculuk insanoğlu için önem kazanmaya başlamıştır. Bu amaç için geliştirilen uzay araçlarında roket motorlarından yararlanılmıştır. Bu araçlarda roket motoru kullanmaktaki amaç dünyanın kütle çekimini yenip uzaya ulaşabilmektir. Roket motorları bu kuvveti gazlardan elde ederler. Kullanılan yakıt türüne göre kimyasal reaksiyonlar sonucu bu gazlar elde edilir ve yüksek hızlarda roketi terkederler. Gazların yüksek hızlarından dolayı oluşan püskürtme etkisi ters yönde itici bir kuvvet uygular ve bu şekilde roketler hareket etmiş olurlar.

Tasarlanan roket motorları kullanılan yakıt türüne göre, katı yakıtlı, sıvı yakıtlı ve hibrit olmak üzere üçe ayrılır. Bunlardan katı yakıtlı roket motorları, yakıtının ucuz olup kolay elde edilebilmesi, kullanım amacına göre farklı büyüklüklerde imal edilebilmeleri, askeri roketlerde kısa sürede hedeflerine ulaşabilmeleri, ateşlemeye hazır halde bekleyebilmeleri, sıvı yakıtlı roketlere göre daha güvenli olmaları gibi sebeplerden dolayı tercih edilmektedirler.

Tez çalışmasında değişken iç geometri içeren bir katı yakıtlı roket motoru (KYRM) bölmesi içinde reaktif akış için basınca bağlı yanma yüzey gerileme simülasyonu içeren bir hesaplama modeli geliştirilmiştir. Kütle, momentum, enerji ve türe ait komple korunum denklemleri sonlu hız kimyası ile çözülmüştür. Mekansal ayrıklaştırma, ikinci dereceden ileri farklar şeması (second order upwind differencing scheme) kullanılarak elde edilmiş ve zamansal ayrıklaştırma birinci derece kapalılık (first order implicit) yöntemi kullanılarak gerçekleştirilmiştir. Sert (stiff) kimyasal çözücü, yüksek sıcaklık gradyeninin yanı sıra maddelerin kütle oranlarının gradyenlerinden dolayı katılık (stiffness) problemini önlemek için kullanılmıştır. Hücreler, alev bölgesindeki akış özelliklerini daha iyi yakalamak için motorun yanan kısmının yakınında yoğun bir şekilde kümelendirilmiştir. Model, yanma yüzeyindeki ses altı girişten lüle çıkışındaki süpersonik çıkışa kadar geniş bir akış Mach sayısı için çözümler üretmektedir. Basınca ve zamana bağlı dinamik sınır, yanan ve gerileyen sınırda oluşturulmuştur. Bunu oluşturmak için ANSYS Fluent 15.0 içinde C++ yardımıyla kullanıcı tanımlı fonksiyonlar (KTF) geliştirilmiş ve kullanılmıştır. Yanma odasının hacmini zamanla arttıran gerileyen sınır, yeniden hücreleme teknikleri ile işlem görmüştür.

Tez çalışması, soğuk akış modelinin doğrulanması, reaktif akış modelinin doğrulanması ve gerileyen sınır durumu için reaktif akış modelleri olmak üzere 3 bölümden oluşmuştur.

Soğuk akışın doğrulanması bölümünde, literatürdeki mevcut Onerac 1 geometrisi için hem sabit hem de gerileyen yanma sınırı için modelleme yapılmıştır. Sabit sınır durumunda roket içi basınç ve Mach sayısı literatürdeki farklı iki çalışma ile

karşılaştırılmış ve uyumlu sonuçlar elde edilmiştir. Bunlara ek olarak akım çizgileri dağılımına bakılmıştır. Kapalı uçtaki basıncın zaman bağlı değişimi de elde edilmiş ve sonuçların literatür ile uyumlu olduğu görülmüştür. Gerileyen sınır durumu için zamana bağlı akım çizgileri 5 farklı an için incelenmiştir. Ayrıca kapalı ucun basınç değişimine de bakılmıştır. Kapalı uçtaki basıncın gerileyen sınır durumunda zamanla azaldığı görülmüştür. Soğuk akış için elde edilen sonuçların literatürdeki çalışmalar ile uyumlu olması gerileyen sınırın başarılı bir şekilde modellendiğini göstermektedir.

Reaktif akış modelinin ele alınıp literatürdeli çalışmalar ile karşılaştırıldığı bölümde ise farklı iki geometri üzerinde çalışılmıştır. Bu bölümde yanma yüzeyi gerilemesi olmamaktadır. İlk durumda bir ucu kapalı dikdörtgen bir kanala yan yüzeylerden propan hava karışımı püskürtülmektedir ve kanal içerisinde akış incelenmektedir. Yanma odası içinde Mach sayısı ve basınç değişimlerine bakılmıştır. Bunlara ek olarak yanma yüzeyinden 2.5 mm'lik uzaklığa kadar olan bölüm incelenmiş ve buradaki sıcaklık ve açığa çıkan ısı dağılımına bakılmıştır. Elde edilen sonuçlar yapılan çalışmanın doğruluğunu göstermektedir. Reaktif akış modelinin ikinci durumunda yine literatürde kullanılan laboratuvar ölçeğinde, çıkışında lüle bulunan bir ucu kapalı dikdörtgen bir kanalda hidrojen hava karışımının kapalı uçtan verildiği bir motor üzerinde çalışılmıştır. 2 mm'lik yanma bölgesi içerisindeki, sıcaklık, hidrojen, oksijen ve su buharı değişimlerine incelenmiştir. Kanal içerisinde sıcaklık ve Mach sayısı dağılımı literatürdeki çalışma ile karşılaştırılmış ve sonuçlar doğrulanmıştır. Bu bölümde de reaktif akışın başarılı olarak modellendiği görülmüştür.

Oluşturulan modelin hem yanma yüzeyinin gerilemesi hem de reaktif akış için doğru sonuçlar vermesinden sonra bu iki model birleştirilerek son bölümde gerileyen yanma sınırı içeren reaktif akış modelleri üzerinde durulmuştur. Burada önce sabit hızla gerileyen ve yanma odası içindeki basınca bağlı olarak gerileyen sınır durumları üzerinde durulmuştur. Sabit hızla gerileme için daha önce kullanılan laboratuvar ölçeğindeki motor çalışılmıştır. Hem propan hem de hidrojen yanması üzerinde durulmuştur. Gerilemenin olduğu ve olmadığı durumlar için sıcaklık dağılımı verilmiştir. Ayrıca farklı hücre boyutları için sıcaklık dağılımlarına bakılmış ve hücre boyutundan bağımsızlık araştırılmıştır. Farklı giriş sıcaklıkları için sonuçlar elde edilmiştir. Hem propan hem de hidrojen yanması durumunda sıcaklık dağılımlarına bakılmış ve maksimum sıcaklıklar karşılaştırılmıştır. Sonrasında itki eğrileri çalışılmıştır. Farklı giriş sıcaklıkları hem hidrojen hem de propan itki eğrileri elde edilmiş ve aynı giriş sıcaklığında bu iki yanma modeli karşılaştırılmıştır. Yanma odası içindeki basınca bağlı sınır gerilemesi modelinde 2 farklı geometri için modelleme yapılmıştır. Bunlardan biri laboratuvar ölçeğindeki motor, diğeri ise Onerac 1 motoru. Laboratuvar ölçeğindeki motor için oluşturulan basınca bağlı gerileyen sınır modelinde zamana bağlı yanma hızı değişimi üzerinde çalışılmıştır. Ayrıca bu, sabit yanma hızı ile karşılaştırılmıştır. Ortam basıncının da zamanla değişimi ele alınmış ve sabit yanma hızındaki değişimi ile karşılaştırılmıştır. Bunlara ek olarak yanma bölgesi içerisinde sıcaklık ve kütlesel oranların değişimi verilmiştir. Önceki bölümlerde olduğu gibi zaman tasarrufu için maksimum hücre boyutu hesaplanmıştır. Sabit ve basınca bağlı gerileme durumlarında sıcaklık değişimleri incelenmiştir. Farklı giriş sıcaklık etkileri üzerine çalışılmıştır. Benzer şekilde hidrojen ve propan yanmaları için sıcaklık değişimleri üzerinde durulmuştur. 2 mm'lik yanma bölgesinde sıcaklık değişiminin akış özelliklerine etkisini araştırmak için bu bölgede hız ve yoğunluk değişimleri çalışılmıştır. Basınca bağlı yanma

yüzeyi gerilemesinin incelendiği ikinci model de Onerac 1 geometrisi üzerinde olmuştur. Burada gerileme sonucu ortam hacminin artmasından dolayı zamanla basınç ve yanma hızı değişimleri elde edilmiş ve bunlar sabit gerileme hızı modelindekilerle karşılaştırılmıştır. Akış ile yanma arasındaki etkileşimi daha iyi inceleyebilmek için yanma bölgesinde dikey ve yatay yöndeki hız değişimleri detaylı bir şekilde araştırılmıştır. Bu bölgedeki hız şiddetinin yatay yöndeki hızdan etkilendiği görülmüştür. Yanma bölgesi içerisinde sıcaklık ve kütlesel oran değişimleri de çalışılmıştır. Uygun hücre boyutu seçmek için farklı boyutlarda sıcaklık değişimleri de incelenmiştir.

Geliştirilen model, değişken iç geometriye sahip bir katı roket motoru yanma odasındaki reaktif akışı basınca bağlı yanma yüzey gerilemesiyle birlikte başarılı bir şekilde temsil etmektedir.

1. INTRODUCTION

The fundamental type of propulsion systems for missile technology used in air defense are solid rocket motors (SRMs). These are devices which convert chemical-thermal energy into kinetic energy. Solid propellant burns through chemical reactions into hot gas mixture inside the combustion chamber in SRM. Ejection of these hot gases from the nozzle with high speed produces thrust and thus propels the rocket forward. For this reason, the control of SRM requires thorough understanding of combustion coupled gas flow associated with regressing solid fuel boundary, which is an extremely complicated phenomenon [1].

Studies on this topic started nearly half a century ago. Early workers studied the gas flow in chamber with cold-flow approach, where inert gases are injected into the chamber. Velocity distributions were obtained analytically for incompressible laminar viscous or inviscid flows in channels [2-8]. Some researchers analyzed the SRM performance with one dimensional steady model [9-10]. Several cold flow experiments were conducted [11-14]. Dunlap et al [15] performed experiments on cold flow field that develops along a cylindrical part of rocket chamber and studied injection driven flow with injection Mach numbers 0.0018 and 0.0036 to achieve centerline Mach numbers of 0.14 and 0.27, respectively. Accordingly, Traineau et. al. [16] conducted cold flow simulation tests of a nozzleless solid rocket motor using a 2-D duct and examined pressure and Mach number variations along this motor. Thereafter, the compressibility effect is illustrated analytically by Balakrishnan et al. [17]. These studies indicate that, the flow Mach number in SRM has a wide range of values. At the injection surface, it starts from approximately 0.001 which is a low value and reaches supersonic conditions at the nozzle. This shows that incompressible and compressible effects coexist in SRM. This issue is one of the challenging sides of numerical modeling of flow in SRM.

The reaction zone is very thin in solid rocket motors, in the order of few millimeters next to the propellant surface and complicated to be described mathematically [18]. Modeling of this thin layer requires challenging computational effort. For this reason, researchers are initially encouraged to model the flow in the chamber as cold flow induced by mass inflow from side porous walls mimicking the burning propellant surface. For example, 2D simulations were studied on a simple cylindrical motor with models representing propellant combustion response by Vuillot et al. [19]. Euler and Navier-Stokes equations were solved in a 2D test case representing SRM using artificial viscosity terms by Lupoglazoff and Vuillot [20]. Kirkkopru and his co-workers solved Navier-Stokes equations numerically in an axisymmetric and cylindrical solid rocket motor chamber to study the generation of vorticity in an injection-induced time-dependent shear flow [21]. Zhao et al. [22] analytically studied the evolution of unsteady vorticity induced by interaction of low Mach number sidewall mass addition and planar axial acoustic disturbances in a cylinder with one closed end. Using a Navier-Stokes solver, an efficient conductive heat transfer model by combining gas flow and heat transfer to the propellant was developed by Alavilli and his co-workers [23]. Various numerical methods are performed for the cold flow simulations [24-36].

The design and the performance of SRMs depends heavily on combustion processes and fluid flow since trust in SRMs is generated through chemical reaction and expansion and acceleration of chemical gas products by passage through a nozzle at the rear of the rocket. Therefore, reactive fluid flow and understanding its characteristics are the important aspects of SRMs. As computational powers increased, researchers started to combine the flow with reaction to reveal reactive fluid flow. The combustion dynamics of SRM with stagnant wall boundaries was studied numerically by Apte and Yang [37]. El-Askary and his co-workers described combustion process in a SRM combustion chamber considering 2D, multi component reactants with turbulent compressible flow [38]. Chu et al. [39], studied unsteady state response of a laminar flame to acoustic waves in a two dimensional combustion chamber with surface mass injection. Yumusak [40] developed a computational method to perform internal flow of two dimensional system using Euler equations. Few researchers dealed with the effects of real gas assumptions for the reacting flow models. [41-49]

The solid rocket motor is the fundamental propulsion concept for both tactical and strategically missiles. Solid propellant is a heterogeneous mixture of an oxidizer, a binder and a metallic powder as a fuel and other additives. An example for the oxidizer is ammonium perchlorate (AP) and for the binder is cured hydroxyl terminated polybutadiene (HTPB). The ballistic behavior of the solid propellant is affected by the burning rate. As combustion takes place, combustion chamber geometry is no longer constant due to the regression of the solid fuel as it turns into the gaseous mixture. Burning area changes result in changes in flow field inside the chamber of rocket motors. Thus, the burning rate of propellants plays a significant role in controlling the parameters such as thrust of rocket motors, and so it is important to model the burning rate in solid rocket motor simulations. [50]. Researchers have worked on solid propellant burning surface regression over the last two decades and this topic is getting more popular over the time. Uygun and Kirkkopru [51] simulated the flow in SRM chamber considering two-dimensional unsteady cold flow with regressing propellant boundary. Terzic and his co-workers [52] conducted numerical simulation of pressure dependent burning surface regression without chemical reactions to predict internal ballistics performance of solid propellant rocket motors. Tola [53] developed a method to enhance the design of optimum missile rocket launchers with improved performance and strength for the internal ballistic analysis of solid rocket motors without reactive flow.

Different definitions are given for the burning rate in the literature [18, 54-58]. For example, it is defined as the regression rate of the solid propellant in parallel layers and perpendicular to the propellant surface [52, 59]. In some studies, it is defined as the distance travelled by the flame front per unit time perpendicular to the propellant surface [60]. The pressure of the combustion chamber, the initial temperature of the solid propellant, the composition of the propellant and the particle size of the oxidizer [18, 52, 56-59] are the main parameters which affect the burning rate. These studies focused on the multi-physics simulation models of SRMs. However, they are limited to relate the regression rate with the flow field via either pressure or temperature. In the present work, a computational method has been developed to simulate chemical reaction coupled with gas flow inside the combustion chamber of SRM with pressure dependent regressive boundary. The model was applied to compressible two-dimensional channel flows. Finite volume discretization

(approach) is utilized and Euler and Navier-Stokes equations with finite rate chemistry are solved with mass, energy and species equations. This reactive gas flow model with constant burning rate was validated against the study by Yumusak [40] in the earlier study of the authors [61].

The chapters are in the following order. In the second chapter, mathematical model including the governing equations and chemical rate expressions are presented in detail. Chapter three covers the numerical model along with solution method. Stiffness problem will be explained in this chapter. The regressive boundary model is discussed comprehensively in this chapter as well. The initial and boundary conditions are presented in chapter four. In chapter five, cold flow numerical results are verified against the Onerac 1 motor for both stagnant and regressing wall. Numerical results for reactive flow with stagnant propellant boundary are verified with flow in a duct with side wall mass injection and in a lab-scale motor as well. Then, cold flow with regressive boundary and reactive flow models are combined and numerical results for reactive flow models with constant and pressure dependent regression velocity models are studied for both lab-scale and Onerac1 motor.

2. MATHEMATICAL MODEL

In this section, conservation equations along with the chemical rate expressions as implemented into the model are presented.

2.1 Governing Equations

The two-dimensional reactive flow model used in this study is based on conservation equations of mass, momentum, energy, and species concentrations for all multicomponents of the chemically reacting system. For a system with N number of species, the governing equations of time dependent Euler equations take the following generic vector form [62]:

$$\frac{\partial Q}{\partial t} + \frac{\partial F}{\partial x} + \frac{\partial G}{\partial y} = H \tag{2.1}$$

where Q, F, G and H are

$$Q = \begin{bmatrix} \rho \\ \rho u \\ \rho v \\ \rho E \\ \rho Y_1 \\ \rho Y_2 \\ \ldots\ldots \\ \ldots\ldots \\ \rho Y_{N-1} \end{bmatrix} \tag{2.2}$$

$$F = \begin{bmatrix} \rho u \\ \rho u^2 + p \\ \rho u v \\ [\rho E + p]u - \rho \sum_{i=1}^{N} h_i D_i \frac{\partial Y_i}{\partial x} - k \frac{\partial T}{\partial x} \\ \rho Y_1 u - \rho D_1 \frac{\partial Y_1}{\partial x} \\ \rho Y_2 u - \rho D_2 \frac{\partial Y_2}{\partial x} \\ \ldots\ldots\ldots\ldots \\ \ldots\ldots\ldots\ldots \\ \rho Y_{N-1} u - \rho D_{N-1} \frac{\partial Y_{N-1}}{\partial x} \end{bmatrix} \tag{2.3}$$

$$G = \begin{bmatrix} \rho v \\ \rho u v \\ \rho v^2 + p \\ [\rho E + p]v - \rho \sum_{i=1}^{N} h_i D_i \frac{\partial Y_i}{\partial y} - k \frac{\partial T}{\partial y} \\ \rho Y_1 v - \rho D_1 \frac{\partial Y_1}{\partial y} \\ \rho Y_2 v - \rho D_2 \frac{\partial Y_2}{\partial y} \\ \ldots\ldots\ldots\ldots \\ \ldots\ldots\ldots\ldots \\ \rho Y_{N-1} v - \rho D_{N-1} \frac{\partial Y_{N-1}}{\partial y} \end{bmatrix} \tag{2.4}$$

$$H = \begin{bmatrix} 0 \\ 0 \\ 0 \\ q \\ s_1 \\ s_2 \\ \dots \\ \dots \\ s_{N-1} \end{bmatrix} \tag{2.5}$$

Here, ρ, u, v, p, E, Y_N represent the total density, x velocity, y velocity, pressure, the total energy and the mass fraction of the Nth species, respectively. h_i is the mass enthalpy for i^{th} species, D_i is the diffusion coefficient and q is the heat of the chemical reaction. Source term, s_N, includes contributions from chemical reactions taking place inside the combustion chamber and it represents the rate of change of every species due to the chemical reaction.

The thermodynamic properties are assumed to be thermally perfect. The specific heat of the species is taken as a function of temperature and perfect gas mixing law is used for the mixture specific heat within the domain. The flow is assumed to be laminar everywhere in the domain. Gravitational force and radiative heat transfer are neglected.

With these assumptions, the conservation equations of mass, momentum, energy, and species concentrations for all multicomponents of the chemically reacting system for a system with N number of species, the governing equations of time dependent equations take the following conservative form in ANSYS Fluent 15.0 [63].

Conservation of Mass

$$\frac{\partial}{\partial t}(\rho) + \nabla \cdot (\rho \vec{v}) = 0 \tag{2.6}$$

Conservation of Momentum

$$\frac{\partial}{\partial t}(\rho\vec{v}) + \nabla \cdot (\rho\vec{v}\vec{v}) = -\nabla p \tag{2.7}$$

Conservation of Energy

$$\frac{\partial}{\partial t}(\rho E) + \nabla \cdot (\vec{v}(\rho E + p)) = -\nabla\left(\sum_{i=1}^{N-1} h_i \vec{J_i}\right) + s_h \tag{2.8}$$

Species Transport Equation

$$\frac{\partial}{\partial t}(\rho Y_i) + \nabla \cdot (\rho\vec{v}Y_i) = -\nabla \cdot \vec{J_i} + R_i \tag{2.9}$$

$$\vec{J_i} = -\rho D_i \nabla Y_i - D_i \frac{\nabla T}{T} \tag{2.10}$$

Where for 2D case

$$\nabla \cdot \vec{v} = \frac{\partial v_x}{\partial x} + \frac{\partial v_y}{\partial y} \tag{2.11}$$

The total energy *E* and total enthalpy *H* are given below.

$$E = h - \frac{p}{\rho} + \frac{\vec{v}^2}{2} \tag{2.12}$$

$$H = h + \frac{\vec{v}^2}{2} \tag{2.13}$$

$$H = E + \frac{p}{\rho} \tag{2.14}$$

$$h = \sum_{i=1}^{N-1} Y_i h_i \tag{2.15}$$

where h is the internal enthalpy. h_i, which is the internal enthalpy of each species, does not influence the other species. It is defined as follows;

$$h_i = \int_{T_{ref}}^{T} C_{p,i} dT \tag{2.16}$$

The sum of all N number of species mass fractions is equal to one. So the mass fraction of the Nth species can be calculated from the below equation.

$$Y_N = 1 - \sum_{i=1}^{N-1} Y_i \tag{2.17}$$

The total pressure is the sum of partial pressures of each species.

$$P = \sum_{i=1}^{N} \rho_i R\, T \tag{2.18}$$

2.2 Chemical Rate Expressions

To close the set of equations, more relations are needed. These relations are thermodynamic and transport properties of the reacting flow system. In this part, the used expressions in the mathematical model for chemical reactive flow in the current work are presented.

The heat of reaction term, which appears on the right side of the energy equation, is as follows:

$$s_h = -\sum_{i=1}^{N-1} \frac{h_i^0}{M_{w,i}} R_i \tag{2.19}$$

R_i is the volumetric rate of creation of species i. For the laminar finite rate model the chemical source term neglects the effects of turbulence and uses Arrhenius expressions. The net sources of the species i due to the chemical reactions are calculated as:

$$R_i = M_{w,i} \sum_{r=1}^{N_r} \hat{R}_{i,r} \tag{2.20}$$

Where $M_{w,i}$ is the molecular weight of each species, N_r is the number of reactions in the chemical model used and $\hat{R}_{i,r}$ is the Arrhenius molar rate of creation or destruction of each species i in each reaction r. The Arrhenius molar rate of creation or destruction of each species $\hat{R}_{i,r}$ is given by [62]:

$$\hat{R}_{i,r} = \left(\vartheta_{i,r}^{''} - \vartheta_{i,r}^{'}\right) k_{f,r} \prod_{i=1}^{N} \left[C_{i,r}\right]^{\eta_{i,r}} \tag{2.21}$$

Where $\vartheta_{i,r}^{''}$ and $\vartheta_{i,r}^{'}$ are the stoichiometric coefficients for product i and for reactant i in reaction r, respectively. $k_{f,r}$, forward rate constant for reaction r and $C_{i,r}$ is the molar concentration of species i in reaction r and $\eta_{i,r}$ is the rate exponent for species i in reaction r. Depend on the chemical model $\vartheta_{i,r}^{'}$ and $\eta_{i,r}$ may take the same value.

The forward rate constant for reaction r is shown below:

$$k_{f,r} = A_r T^{\beta_r} e^{-E_a/RT} \tag{2.22}$$

where A_r is the pre-exponential factor, β_r is the temperature exponent, E_a is the activation energy of the reaction and R is the universal gas constant.

$$D_{i,m} = \frac{1 - X_i}{\sum_{j,j\neq i}^{N} \left(X_j / D_{i,j} \right)} \tag{2.23}$$

where X_i represents the mole fraction of species i, $D_{i,j}$ is the binary mass diffusion coefficient of component i in component j. The specific heat Cp is calculated for every species i using temperature dependent polynomial function.

$$C_{p,i}(T) = \sum_{k=0}^{m} a_{k,i} T^k \tag{2.24}$$

where a_k is the polynomial coefficient. For the mixture specific heat, the following mixing law is used.

$$C_p = \sum_{i=1}^{N} Y_i C_{p,i} \tag{2.24}$$

If the flow is cold flow, the source term R_i, which is the volumetric rate of creation of species i, takes the value of zero for every species. In this case, the source term s_h in the energy equation drops.

3. NUMERICAL MODEL

In this chapter, numerical algorithms improved for the solution of the governing equations with finite rate chemistry as well as regressive boundary model are demonstrated. Firstly, the solution method is investigated comprehensively along with the models used. Then, the stiffness problem in the combustion model is presented briefly. Finally, the regressive boundary model is explained in detail with the methods used.

3.1 Solution Method

The governing equations coupled with the chemical reactions are solved using the commercial software ANSYS Fluent 15.0 [63]. The combustion is treated using finite rate chemistry model. Spatial discretization is obtained using second order upwind differencing scheme and temporal discretization is achieved using first order implicit method.

Temperature and species mass fractions vary very rapidly within a very thin zone adjacent to the boundary mimicking the propellant surface. Thus, to better capture these rapid variations of flow properties within this thin regime, cells are highly clustered in the neighborhood of the end burning part of the motor as were done by others [23, 37, 39, 51]. Figure 3.1 illustrates an example for the computational grids near the head end of the computational domain in lab-scale motor used in this study. The smallest cell which is next to the transpiring left-hand wall is taken 0.015 mm thick. The dimensions of the subsequent ones in axial direction are set to be 1.05 times the previous one that is the growth factor is 1.05. This sizing strategy in gridding holds till 30 mm away from the head end boundary. Beyond this distance onwards, the sizes of the grids are taken uniform. 50 uniform and 224 non-uniform grids are used in the vertical and horizontal directions, respectively. Under-relaxation factor of 0.7 within each time step is used for pressure, momentum and temperature for numerical stability.

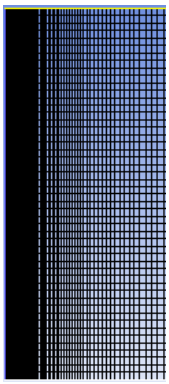

Figure 3.1 : Grid structure next to the end-burning boundary in the lab scale motor.

The convergence residuals for continuity, velocity, energy, and mass fractions of the species are set to be 10^{-3} for every iteration in each time step for unsteady calculations in all cases. When the steady state results are obtained, the absolute residual of energy and velocity are $4x10^{-5}$ and $8x10^{-5}$, respectively.

Steady state calculations are carried out by setting the temperature at all grid points equal to the adiabatic flame temperature of the combustion model, initially. Accordingly, velocity field and species mass fractions in the domain are taken equal to the inlet velocity and species mass fractions at the end burning boundary. For some cases, the numerical solutions diverged while using the Euler equations. Therefore, first the flow field is solved using the Navier-Stokes equations, then these solutions are taken as the initial conditions for the Euler type model. Non-regressive and regressive boundary models will be explained in the following parts.

3.2 Stiffness Problem

Stiffness is the main issue that makes the combustion models more challenging. It was first recognized by Curtiss and Hirschfelder [64]. High levels of stiffness may cause to reduce the performance of numerical model or destroy the model completely. For a system with chemically reacting flow, stiffness originates from the temperature and concentration dependent source term S_N. The principal problem arises from the temperature variations, since the source term S_N depends on the temperature exponentially. This exponential dependence makes the source term significantly stiff. If the source terms of the species are large, they generate rapid spatial and temporal changes in the dependent variables, which are mainly temperature and species mass fractions. These changes lead to wide range of

chemical time scales. In addition to these, fluid dynamics time scales should be considered as well. All these time scales mostly cause problems in solution models. To avoid this problem, stiff chemistry solver option is used in ANSYS Fluent 15.0 [63]. This method can be used for both pressure based solver and density based solver. For the unsteady simulations with pressure based solver, the stiff chemistry solver follows a fractional step algorithm [63]. In the former step, using the ISAT integrator, the chemistry is calculated in each cell at constant pressure for the flow time step. In the latter one, the convection and diffusion terms are treated as in a cold flow simulation. The solution is more stable with the stiff chemistry solver for the density based solver as well.

3.3 Regressive Boundary Model

SRM has a variable internal geometry due to the transformation of the solid propellant to form combustion products. This variation in geometry is called surface regression. Changing combustion volume in time results in change of pressure and thrust and thus causing a change in SRM performance.

In the present study, surface regression is modeled with a layer between solid propellant grain and the gases which are the fuel-air mixture as shown in Figure 3.2 as in the study of [65]. The left part is solid fuel with oxidizer. The thin red zone is the layer where solid fuel is vaporized to form reactant and oxidizer gases. Therefore, it is assumed that the reaction starts at the interface between the red zone and the chamber. As combustion occurs, the amount of the solid fuel decreases and the boundary regresses to the left. Displacement of the burning surface is considered as parallel layers normal to burning surface of the propellant grain [52, 59, 61]. The movement of this boundary is governed by the burning rate $\dot{r}_b$.

As surface regresses with burning rate $\dot{r}_b$, the reactant and oxidizer gases leave the burning surface in opposite direction with the velocity V_g. Since the propellant density ρ_p is much higher than the density of the gaseous reactant and oxidizer mixture ρ_g, the velocity of this mixture is significantly greater than the burning rate. Thus, conservation of mass is approximately [65]:

$$\rho_p \dot{r}_b \approx \rho_g V_g \tag{3.1}$$

Here the velocity V_g or the mass flux $\rho_g V_g$ can be determined through Equation (3.1), because the density of the propellant is known and the burning rate of the regressing boundary can be calculated using the below Equation (3.2).

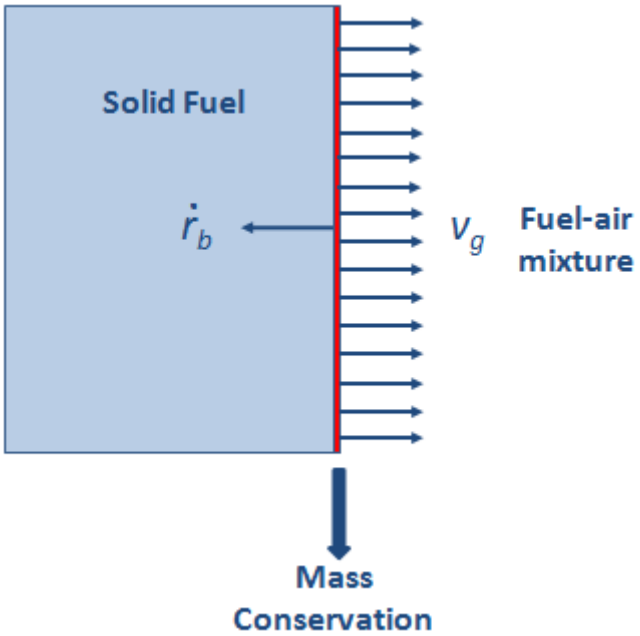

Figure 3.2 : Surface regression model [65].

There are several parameters which affect the burning rate. These are the pressure of the combustion chamber, the initial temperature of the solid propellant, the composition of the propellant and the particle size of the oxidizer. In this study, constant burning rate and pressure dependent burning rate are investigated.

In the literature, some formulations are offered to predict the burning rate of an energetic solid propellant [18,52,56-59]. One of the well-known formulations is the APN model, which approximates the burning rate as solely dependent on the mean local pressure within the combustion chamber [52].

In the current study, the burning rate of the solid propellant is simulated using the APN model as follows;

$$\dot{r}_b = \alpha p^n \tag{3.2}$$

This is known as Saint Robert's law or Vieille's law [65, 66]. In this equation, $\dot{r}_b$ is the pressure dependent burning rate. α is a constant which depends on the initial temperature of the solid propellant. It has a value between 0.002 and 0.05 [65]. p is the chamber pressure. n is the pressure index which strongly depends on the type of

the propellant. For double base propellants n has a value between 0.2 and 0.6 [65]. For ammonium perchlorate it takes the value between 0.1 and 0.4 [65]. The values of α and n cannot be predicted theoretically. They are determined experimentally. For a particular propellant, minimum of five tests using propellant strands at constant pressure is used for determining the values of α and n. These tests should be performed at minimum three different pressures. [60]

In order to numerically model the regression of the burning surface boundary, user-defined functions (UDF) are customized using C++ [67] and implemented in ANSYS Fluent 15.0 [63]. Displacement of the boundary is considered only perpendicular to the boundary surface. With this assumption, the end burning boundary regression is calculated using the below expression:

$$x_{new} = x_{old} - \dot{r}_b \Delta t \tag{3.3}$$

Here, x_{new} is the calculated new x-coordinate of the boundary at the end of the time step Δt, whereas xold is the x-coordinate of the boundary in the previous time step. $\dot{r}_b$ is the burning rate.

For the constant burning rate simulations, the UDF "DEFINE_GRID_MOTION" is used to move the regressive burning solid propellant boundary. It is customized in C++ [67] so that at the end of every time step, the new location of the moving boundary is calculated using the Equation (3.3) and then updated using the mentioned UDF. In the simulation of lab-scale motor, which will be explained later, new vertical uniform grid lines are added in the horizontal direction during the unsteady combustion process with regressive boundary. This method is named as Dynamic Layering Method in ANSYS Fluent 15.0 [63]. This method allows specifying a desired layer height next to the moving boundary. There are two options for the layering method which are constant height and constant ratio procedure. In the current study, constant height option is chosen. In the simulation of Onerac 1 geometry, which will be investigated later as well, the same UDF is used to move the boundary. During the regression of the boundary Local Cell Remeshing technique is used because triangular grids are used. In this method, where the boundary displacement is large compared to the local cell heights, the cell quality can be destroyed and this may result in negative cell volumes [63]. This problem leads to convergence problems. To prevent from this issue, ANSYS Fluent 15.0 [63]

accumulates the cells that violate the skewness and locally remeshes the agglomerated cells. The solver comments each cell and notes it for remeshing when it meets one of the criteria below:

- It is higher than the desired minimum cell height
- It is shorter than the desired maximum cell height
- Its height does not compensate the desired length scale
- It has a higher skewness value than the desired maximum skewness value

If the new cells assure the skewness criteria, the new mesh is updated with the new one.

For the pressure dependent burning rate simulations, the following UDF's are added to the solver. These are "DEFINE_EXECUTE_AT_END" and "DEFINE_PROFILE". At the end of the every time step, the UDF "DEFINE_EXECUTE_AT_END" is called in order to calculate the average pressure in the combustion chamber. Using the pressure dependent burning rate expression which is proposed by Vieille, the burning rate of the solid fuel is calculated with the mentioned UDF. Since the density of the propellant is known, the inlet velocity on the burning boundary is calculated. Then the "DEFINE_PROFILE" UDF is called in order to update the velocity inlet at the solid fuel boundary. Finally the "DEFINE_GRID_MOTION" is performed to move the regressing boundary with the calculated burning rate in the time step. After all of these calculations have been done, the solver continues to iterate to the next time step. This procedure is carried out until all the solid fuel is consumed.

4. INITIAL AND BOUNDARY CONDITIONS

After the governing differential equations are discretized both spatially and temporarily, the solution starts from an initial state condition subjected to boundary conditions describing the geometry. Then, the equation system is integrated in time to reach a steady or for an unsteady solution depending on the problem.

Initial conditions have to be provided in order to start the solution. A good initial condition helps to get fast convergence for the numerical scheme. For internal flow as in this study, the initial conditions everywhere in the domain are specified to be equal to the inlet conditions. However, there are some exceptions in the initial conditions for temperature field, which will be discussed later.

Boundary conditions play an important role in any numerical simulation in the sense of both stability and accuracy of the numerical scheme. After the set of partial differential equations describing the model are set and physical boundaries are specified, the boundary conditions can be implemented. Then these boundary conditions are expressed mathematically.

In the following section, inflow, solid wall, symmetry and outflow boundary conditions which were used to describe the 2D SRM will be explained.

4.1 Inflow Boundary Conditions

Inflow boundary is used for the inlet mass flux at the injecting boundary. At this boundary, the mass flux, temperature of the mixture and the species mass fractions are specified to compute the injection velocity and density at the boundary. The velocity, which is perpendicular to the subsonic inlet direction, is assumed to be zero.

The density is calculated from:

$$\rho_{inj} = \frac{p}{RT_{inj}} \tag{4.1}$$

Since the mass flux is specified and the density is known, one can calculate the injection velocity from

$$Mass\ Flux = \rho_{inj} V_{inj} \tag{4.2}$$

In the simulations with propellant regression, the burning propellant surface with an inlet boundary condition moves with a velocity which corresponds to the burning rate of the propellant, which was discussed in regressive boundary model section in Chapter 3.

4.2 Adiabatic Solid Wall Boundary Condition

Wall boundary conditions are used to bind the fluid and the solid regions in the simulated domain. Adiabatic wall represents no heat transfer through the wall. In the solid wall boundary condition, if the model is based on an inviscid flow, no flow normal to the wall surface is assumed. In this case, there is no friction force. The velocity vector is tangent to the surface. The values of the conservative variables are extrapolated from the interior points.

If the flow is viscous, there is no-slip boundary condition, and velocity components become zero at the wall surface.

4.3 Symmetry Boundary Condition

For a symmetry boundary, there is no flux across the boundary. The normal component of the velocity at the symmetry boundary is set to be zero. The normal gradients of all flow variables are assumed to be zero at this boundary.

4.4 Outflow Boundary Condition

Outflow boundary conditions are used to predict the flow variables at the exit, where these variables are unknown prior to solution. Depending on the simulation, the outflow boundary conditions for a SRM are mostly supersonic. For this case, the flow quantities such as velocity, temperature, species mass fractions and density on the outflow boundary are extrapolated from the interior cells.

5. RESULTS AND DISCUSSION

In this chapter, numerical results obtained from the current study are presented. Computed results are compared to the numerical ones in the literature when available.

Firstly, cold flow model is computed and validated with and without regression of the propellant boundary in this study. Secondly, reacting flow simulations without moving boundaries are examined and verified against two different studies [39, 40]. Then, the model is further developed for reacting flow including constant and pressure dependent burning boundary regression of the solid propellant boundary. Two different cases, lab-scale motor and Onerac 1, are studied.

5.1 Cold Flow Validation

5.1.1 Onerac 1 with non-regressive boundary

The first case is known as the Onerac1 [20] in the literature. It is a two dimensional channel with sidewall mass injection as shown in Figure 5.1. It is closed at one end (head end) and has a nozzle on the right end. The overall motor length is 470 mm and the half height is 45 mm. The propellant surface is 200 mm long and its thickness is 15 mm. It has a 70 mm converging-diverging nozzle with a radius of curvature 30 mm.

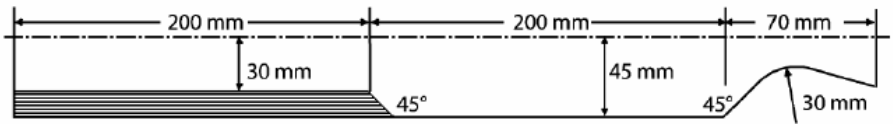

Figure 5.1 : Geometry of Onerac 1 [51].

For computational domain, 328 x 32 grids are used for the cold flow case as shown in Figure 5.2. The density of the grid is increased after the propellant part of the chamber as does the study of [68]. The spacing of the first grid next to the injecting wall is 0.011 times the half height of the chamber.

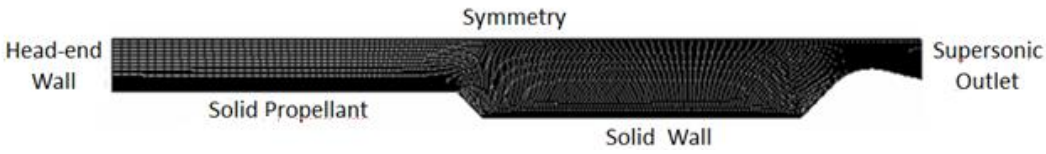

Figure 5.2 : Computational domain of Onerac 1 with boundary conditions [68].

Air, with a mass flux of 21.201 kg/(m^2s) and temperature of 3387 K, is injected from the propellant surface into the chamber.

First, steady state Euler solutions are obtained using the Software Ansys Fluent 15.0 [63]. Then, these steady results are used as initial condition to obtain the unsteady head-end pressure change for non-regressive boundary model as done by Uygun [68].

Pressure, Mach number and streamline contours are presented for the steady Euler solutions. Figure 5.3 shows the pressure distribution comparison along the chamber. In the propellant section, the pressure drops from 4.6 bar to 4.1 bar. Between the propellant and the entrance of the nozzle the pressure remains almost constant. From the throat of the nozzle to the exit, pressure decreases. Good agreement has been obtained with the present work when compared to results of the studies of [20, 68].

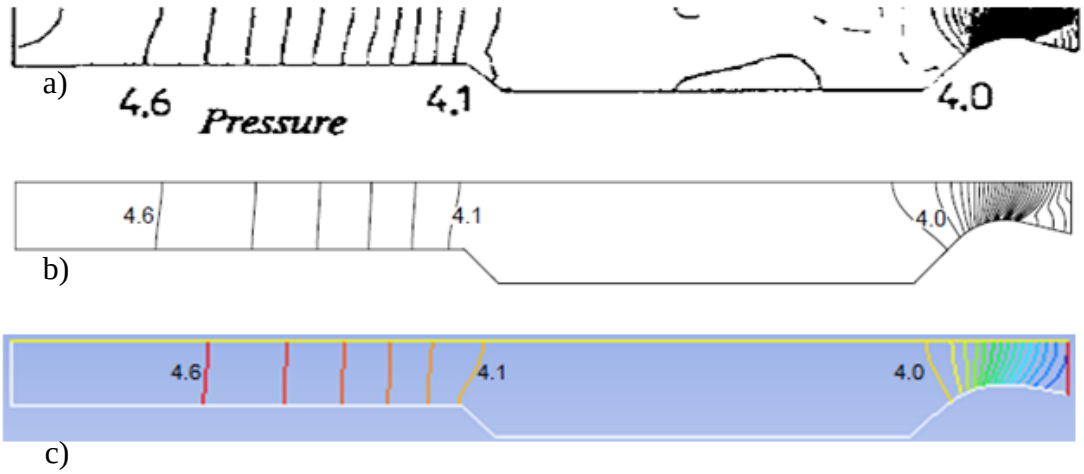

Figure 5.3 : Comparison of pressure contours (bar) a) Work of Vuillot [20] b) Work of Uygun [68] c) Current study.

Mach number contours comparison is demonstrated in Figure 5.4. Mach number contours show that the flow accelerates along x direction and takes the sonic value at the throat of the nozzle. It has a maximum value of 1.9 at the exit of the nozzle. The present study and the works of [20, 68] have similar results except slight differences

in the exit of the nozzle. This is attributed to different numerical treatments in the solution.

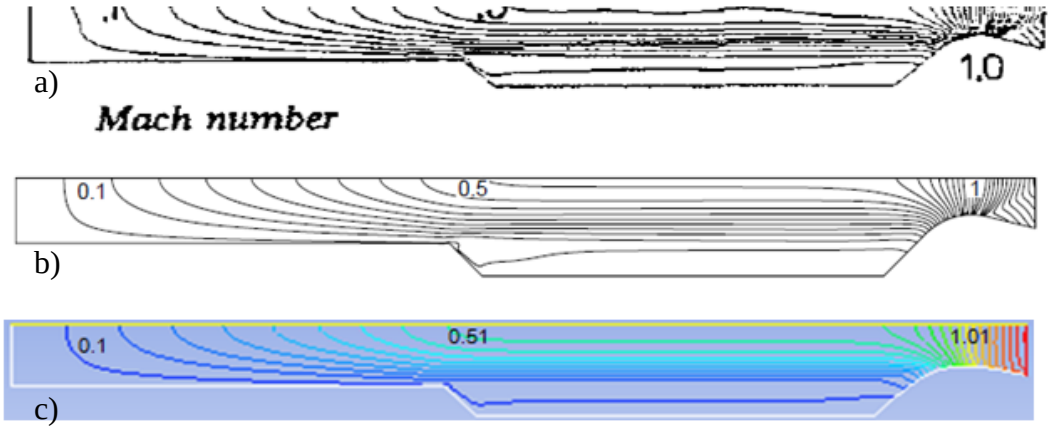

Figure 5.4 : Comparison of Mach number contours a) Work of Vuillot [20] b) Work of Uygun [68] c) Current study.

The streamlines are compared in Figure 5.5. Since there is no data in the referenced work, only the streamline contours are presented.

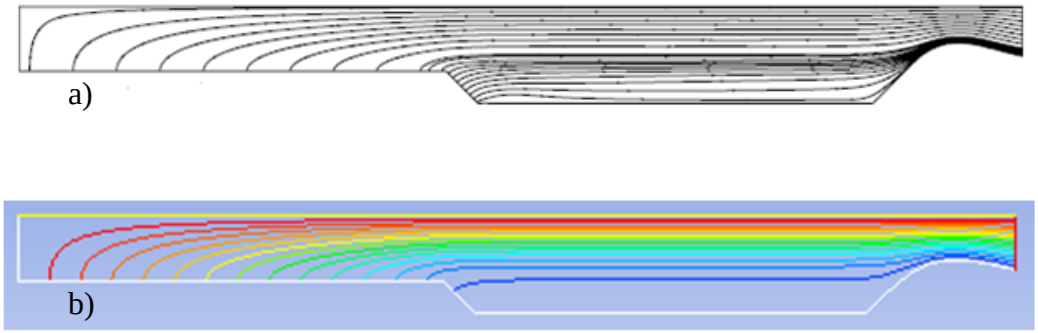

Figure 5.5 : Contours of streamlines a) Work of Uygun [68] b) Current study.

Figure 5.6 demonstrates the time history for the head-end pressure both for the current study and the work of [68] for unsteady non-regressive boundary model. As it is seen from the figure, the pressure oscillates in time in both studies. The amplitude in the current study is smaller compared to the study of Uygun [68]. This may be due to the different intensities of the artificial viscosities used in the studies.

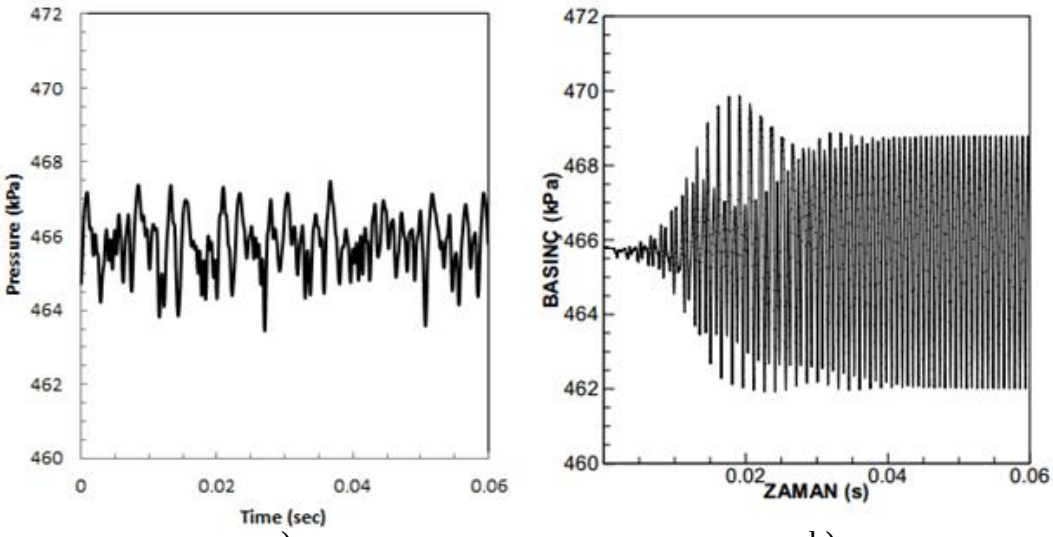

a) b)

Figure 5.6 : Time history of head end pressure a) Present work b) Work of Uygun [68].

5.1.2 Onerac 1 with regressive boundary

In this section, results obtained from unsteady constant regressing rate simulation are demonstrated. The steady state Euler results obtained for non-regressive boundary are used as initial condition for the unsteady computation of the cold flow simulation for constant regressing rate boundary model as done by Uygun and Kirkkopru [51].

Figure 5.7 shows the streamline contours for the current study as well as the work of [68] using constant rate regressive boundary model for different times. There exist no numerical data in the referenced study; therefore only streamline contours are presented. Both studies display similar trends for the given time instants.

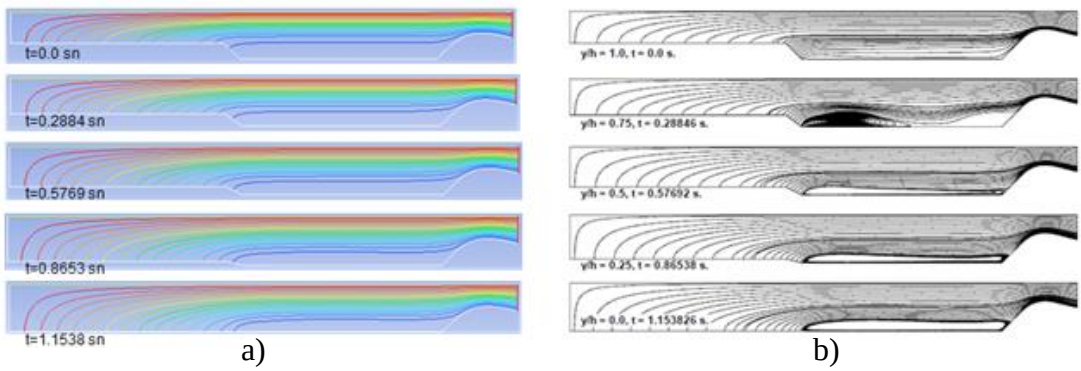

a) b)

Figure 5.7 : Streamlines comparison during the propellant regression a) Present work b) Work of Uygun [68].

The time history for the head end pressure is compared for both the current study and work of [68] in Figure 5.8. The pressure starts to decrease from 465 kPa at the head end. When all the solid propellant is consumed, which is at t=1.15 s, the head end pressure is 438 kPa in the current study and 439 kPa in the study of Uygun [68]. The pressure decrease during the solid propellant regression is about 5.8 %. For pressure dependent regression model, the change in pressure will be an important parameter for the motor performance.

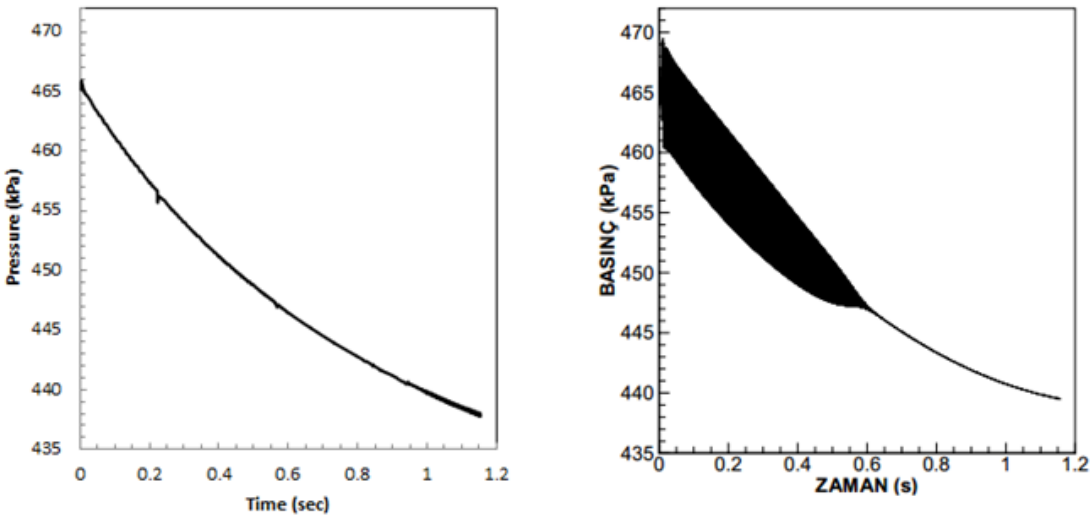

a) b)

Figure 5.8 : Time history for head-end pressure a) Current work b) Work of Uygun [68].

5.2 Reacting Flow Validation

Numerical results demonstrated in this section validate the accuracy and the computational efficiency of the reacting flow simulation for non-regressive boundary regression in SRM. Two different geometries are performed. These cases are two dimensional duct flows, one of which is a rectangular combustion chamber including a head end with sidewall mass injection without a nozzle and the other one is an end burning lab-scale motor with a nozzle.

5.2.1 Flow in a duct with side-wall mass injection

The current case is a two dimensional planar rectangular model which is shown in Figure 5.9. The chamber has an aspect ratio of 20, which is 1 m in length and 0.05 m in half-height. The chamber is closed at the head end. Premixed fuel-air mixture is

injected from the bottom surface. Due to the model geometry, upper part is symmetry boundary condition. Left side is solid wall and the combustion products leave the chamber from the right side. It is numerically simulated in [39]. A similar test case was experimentally studied by Sankar et al [69]. This configuration represents the flow in SRM combustion chamber, where side wall mass injection simulates the addition of combustion gases into the flow stream.

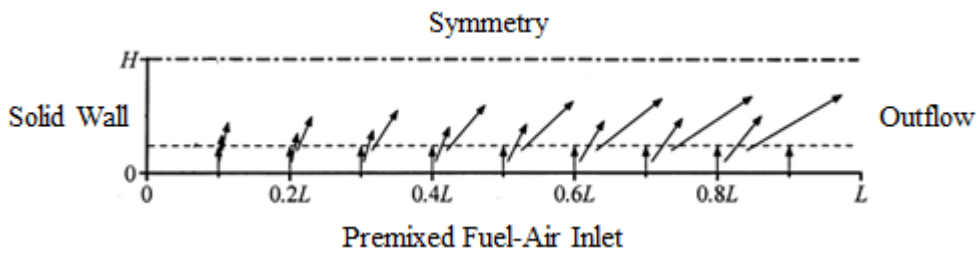

Figure 5.9 : Geometric representation of the side wall mass injection [39].

The computational grid is illustrated in Figure 5.10. It consists of 60 x 100 non-uniform cells in x and y directions, respectively. Due to the high temperature and species mass fractions gradients, cells are clustered more closely next to the mass injection wall. The first grid thickness just above the boundary is 0.015 mm.

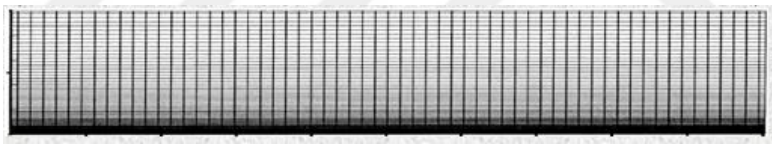

Figure 5.10 : Non-uniform grid extending from the mass injecting wall to the symmetry line [39].

The gaseous combustion products leave the chamber at the aft end. Propan-air mixture with an equivalence ratio of 0.7 is injected at a flow rate of 0.21 kg/m^{2}s as does the study of [39]. The injecting temperature is 350 K.

Figure 5.11 compares the Mach number contours throughout the chamber both for the current work and the study of [39]. The contours show the typical structure of an injection driven flow. The flow Mach number increases almost linearly along the symmetry boundary from zero at the head end and to 0.044 at the exit for both studies. This change is consistent with cold flow predictions for a similar chamber [70]. The calculated injection velocity is 0.206 m/s which agree with the study of [39]. This value agrees well with the experimental value of 0.209 m/s reported by [71]. In addition to the injection velocity, calculated surface Mach number of

$5.6x10^{-4}$ is compatible with the referenced study [39]. Finally, velocity of the gas mixture increases to a speed of 1.145 m/s in the current study; close to 1.154 m/s in the study of [39].

a)

b)

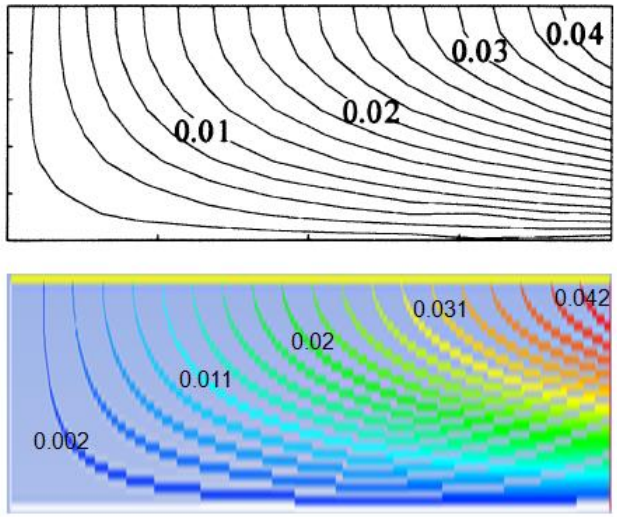

Figure 5.11 : Comparison of Mach number contours a) Study of Yang [39] b) Current study.

The pressure contours represent an almost one dimensional distribution in Figure 5.12. No recognizable variation is observed in the y direction. Only small changes are seen near the injecting wall due to the volume expansions in the flame zone. The pressure decreases from 128 Pa at the head end to almost zero at the exit. The results of the current study show consistency with the study of [39].

a)

b)

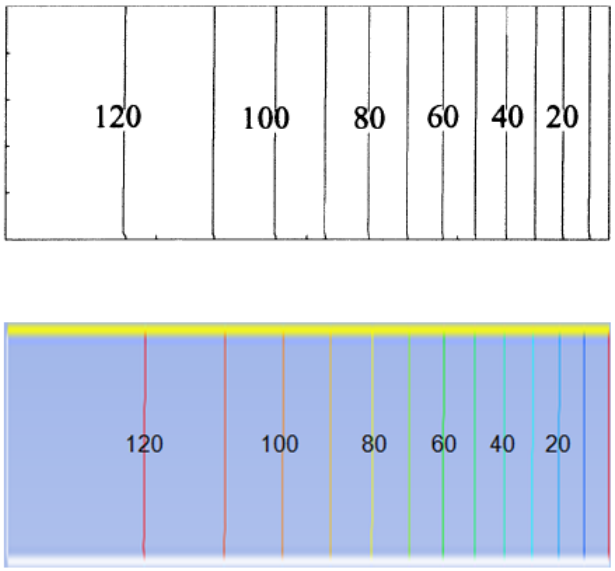

Figure 5.12 : Comparison of pressure contours (Pa) a) Study of Yang [39] b) Current study.

To validate the chemical model, the temperature and heat of reaction distributions are presented in Figure 5.13 and compared with the work of [39]. It is observed that, at every location on the injecting wall the temperature increases drastically in the y direction. The variations in temperature are in negligible order, because the heat of reaction along the injecting surface is uniformly distributed and the characteristic Mach number is at the order of 10^{-2}. The temperature increases from the injecting value of 350 K to a maximum value of 1922 K in the current work and 1938 K in the study of YANG [39]. The maximum value is observed just past the flame edge at y=2 mm in both studies. The calculated flame temperature of 1922 K agrees well with the chemical equilibrium result of 1915 K studied by NASA CET93 code [72]. In addition, the heat of reaction curves show similar trend in both studies. They take the peak value, where the highest temperature gradient starts to decrease.

a)

b)

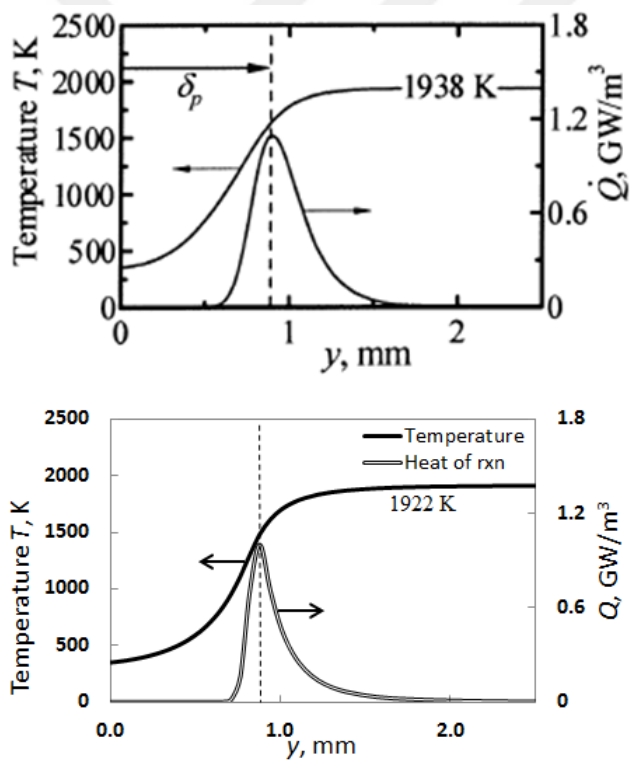

Figure 5.13 : Comparison of temperature and heat release variations a) Study of Yang [39] b) Current study.

5.2.2 Flow in a duct with end-burning mass injection

The current case includes inviscid laminar reacting flow simulation in a two dimensional duct. Figure 5.14 illustrates a schematic combustion chamber of this

SRM. The model is a 2-D end-burning lab-scale motor, which has a chamber length of 170 mm. The half-height is 45 mm. This chamber is connected downstream to a converging-diverging nozzle with a half throat height of 16.77 mm and radius of curvature of 30 mm. The model length including the nozzle is 270 mm. The gaseous H_2 premixed with O_2 is injected at low Mach number subsonic conditions from the head-end surface perpendicular to the main stream, mimicking the combustion in solid propellant surface.

There are four boundary conditions for the lab-scale model. The left side of the model, which is the end-burning part, is taken as a subsonic inlet. The mass flux at this injecting boundary is 11.39 kg/m^{2}s and the injection temperature is 3387 K as in the study by Yumusak [40]. The fuel-air equivalence ratio is 0.3. The upper part has a symmetry boundary condition. The velocity in y-direction is set to be zero at this boundary. The lower solid impermeable boundary and the nozzle wall are adiabatic. The gaseous mixture leaves the nozzle at supersonic conditions. For supersonic outflow the flow properties are calculated from the interior points.

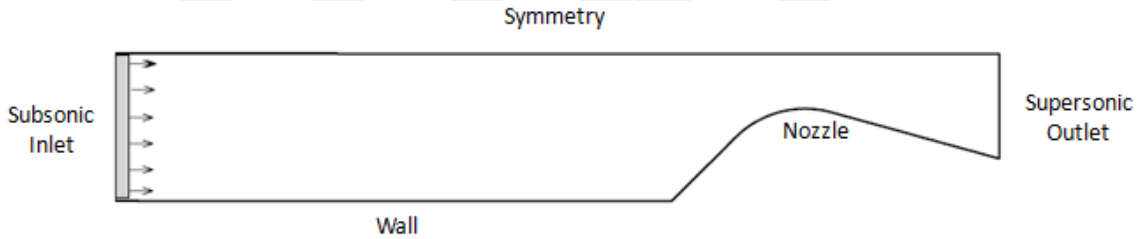

Figure 5.14 : Geometric representation of the lab-scale motor [40].

As explained before, thermodynamic properties are thermally perfect. The specific heats of the species are taken as a function of temperature. Thermal conductivity is taken constant for the gaseous mixture. Additionally, gravitational force and radiative heat transfer are neglected. The flow is assumed to be laminar everywhere in the domain.

Despite the recent developments in computational resources, thorough consideration of all physical and chemical processes in SRM and modeling of those are still challenging. A simplified reaction mechanism can therefore be considered to describe the combustion process. In this model, a chemical model based on the combustion of hydrogen gas with air is considered. Hydrogen combustion process is assumed to follow a two-step model, where in the first step hydrogen reacts with oxygen to form hydroxide and in the latter hydroxide combines with hydrogen to

compose gaseous water molecule. This reaction mechanism has been well established and captures information about the major chemical kinetic pathways. It can be represented by the following steps [73].

$$H_2 + O_2 \leftrightarrow 2OH$$

$$2OH + H_2 \leftrightarrow 2H_2O$$

Steady state calculations are achieved by setting the temperature at all grid points equal to the adiabatic flame temperature of the combustion model, initially. Accordingly, velocity field and species mass fractions in the domain are taken equal to the inlet velocity and species mass fractions at the end burning boundary. The numerical solutions diverged while employing the Euler equations. Therefore, first the flow field is solved using the Navier-Stokes equations, then these solutions are taken as the initial conditions for the Euler type model. The final steady state solutions are obtained using the time marching technique offered by the software Fluent 15.0 [63]. Non-regressive boundary model results are verified with the inviscid non-regressive study of Yumusak [40].

The chemical reaction of the fuel air mixture in a very thin flame zone close to solid propellant surface is shown in Figure 5.15. Within this flame zone, the variations of flow properties such as temperature and species mass fractions are very rapid. The temperature increases from the feeding boundary temperature of 3387 K to 3807 K in a distance less than a millimeter. The flow characteristics within this region are captured using grids that are highly clustered near the end burning part of the motor. Figure 5.15 also compares mass fractions of H_2, O_2 and H_2O species along the axis of the combustion chamber. H_2 and O_2 mass fractions decrease from 0.0083 and 0.22 corresponding the equivalence ratio 0.3 to 0.0001 and 0.155, respectively. The mass fraction of the product, H_2O, increases from 0 to 0.07.

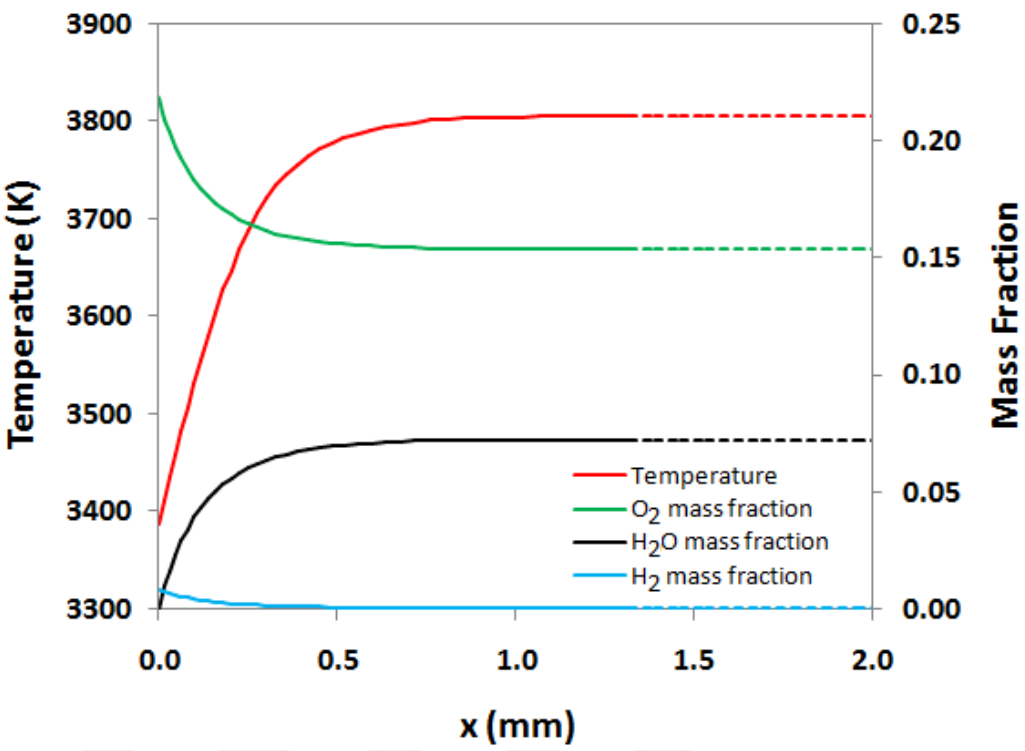

Figure 5.15 : Temperature and mass fractions along x-axis from the burning end.

Figure 5.16 represents the temperature contours for both present and Yumusak's study [40]. With an inlet temperature of 3387 K the temperature of the mixture increases to 3807 K. The thin flame zone is not observed in this figure, since this zone is very small compared to the size of the combustion chamber. After the chemical reaction takes place, the maximum temperature is achieved 3807 K in the present study which is very close to the value of 3804 K in the work of Yumusak [40]. All the way down to the inlet of the nozzle, the temperature remains nearly constant since the chamber wall is adiabatic. Close by the throat of the nozzle, the temperature starts to decrease. The temperature contours match for both studies except in a small section of the diverging part of the nozzle possibly due to different numerical treatments. Temperature takes value around 2400 K at the exit of the motor for both studies and temperature variations in product gas flow are at the order of M^2. M is the characteristic flow Mach number which is less than 0.2 in the chamber.

Figure 5.16 : Comparison of temperature contours a) Contour map from the work of Yumusak [40] b) Contour map from the current study.

The comparison of Mach number contours in the present study with those obtained by Yumusak [40] is shown in Figure 5.17. The Mach number remains almost constant through the rectangular part of the channel as does the temperature. As the flow enters the nozzle the Mach number starts to increase and reaches the sonic value at the nozzle throat for both studies and contours look similar except in the small section of the diverging part of the nozzle as do the temperature contours. Mach number takes the maximum value of 2.10 at the exit of the nozzle in the current study whereas it takes 2.06 in the referenced study [40].

Figure 5.17 : Comparison of Mach number contours a) Contour map from the work of Yumusak [40] b) Contour map from the current study.

5.3 Reacting Flow with Regressive Boundary Computations

SRM has a variable internal geometry due to the transformation of the solid propellant to reactant and oxidizer to form combustion products. This variation in geometry with changing combustion area in time results in change of pressure and thrust and thus causing a change in SRM performance.

In this section, numerical results obtained from the regressive boundary models including reacting model will be presented. Firstly, constant regression rate model for the lab-scale motor is illustrated. Then, pressure dependent regression rate for the same geometry is investigated. Finally, Onerac 1 case [20,68] is used to model the reactive flow model containing pressure dependent burning rate.

5.3.1 Constant rate regressive boundary model for lab-scale motor

Once steady state reactive flow solutions are obtained and validated without regression on the end burning boundary, more complex SRM modeling is imposed through numerical model. In this part, the same geometry as that without regression is considered. Figure 5.18 illustrates a schematic combustion chamber of the lab-scale motor including the attached solid fuel. Boundary conditions are taken same as the previous case except the inlet temperature and the equivalence ratio on the end boundary. In this case, two different inlet temperatures, 350 K and 800 K, are considered with equivalence ratio of 0.7. First, non-regressive model with chemical reaction model is solved until steady state results are obtained for the prescribed inlet temperatures. Then, these steady results are set as initial conditions for the unsteady numerical calculations with regressive boundary, as done by others [68]. The density of the propellant is taken 1633 kg/m^3 [51] and the corresponding burning rate is 6.97x10^{-3} m/s. The computational model for this case is explained in Chapter 3.

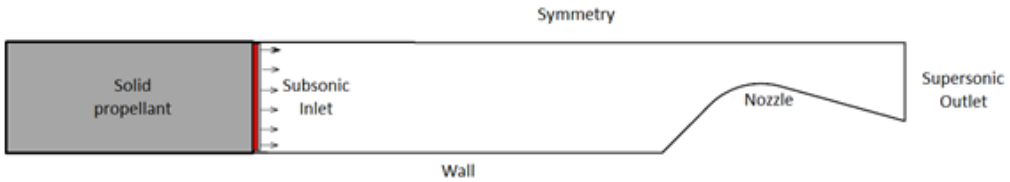

Figure 5.18 : Geometric representation of the lab-scale motor with attached solid fuel.

Boundaries are a symmetric upper boundary, an impermeable lower wall and the burning head end. The gaseous mixture leaves the combustion chamber through a nozzle at supersonic conditions. On the head-end, propellant surface degrades as it burns.

To numerically model the regression of the burning surface boundary, the UDF "DEFINE_GRID_MOTION" is used to move the regressive boundary. Displacement of the boundary is considered only in x direction. With this assumption, the end burning boundary regression is calculated using the below expression:

$$x_{new} = x_{old} - \dot{r}_b \Delta t \tag{5.1}$$

x_{new} is the calculated new x-coordinate of the boundary at the end of the time step Δt. x_{old} is the x-coordinate of the boundary in the previous time step. $\dot{r}_b$ is the constant burning rate. At the end of every time step, the location of the moving boundary is calculated and updated. New rectangular grids are added to the left of the computational domain for every regression distance of 0.03 mm. The initial thickness of the propellant 100 mm is added to the total length of 270 mm. Given the constant burning rate of 6.97×10^{-3} m/s, the propellant is consumed in 14.35 seconds. During the unsteady combustion process with regressive boundary new vertical uniform grid lines are added in the horizontal direction.

Numerical simulation of regression of the end burning boundary is examined in a 2D transient, laminar, reactive flow model with two different chemical models. The former one is hydrogen combustion used in the previous model. The latter one is the combustion of propane, which is assumed to follow a one-step reaction, which yields carbon dioxide and water vapor as products [63].

$$C_3H_8 + 5O_2 \rightarrow 3CO_2 + 4H_2O$$

Using this simulated model, effects of regressive boundary on temperature profile, velocity profile in the axial direction for H_2 combustion and SRM thrust curves for both H_2 and C_3H_8 chemical models are studied.

Figure 5.19 illustrates the temperature profiles both for no regression and 1 mm regression of the solid fuel boundary with inlet temperature of 350 K. Considering an equivalence ratio of 0.7 for H_2 combustion, the temperature reaches a maximum

value of 1918 K in both models indicating that the chemistry is not affected from the boundary regression.

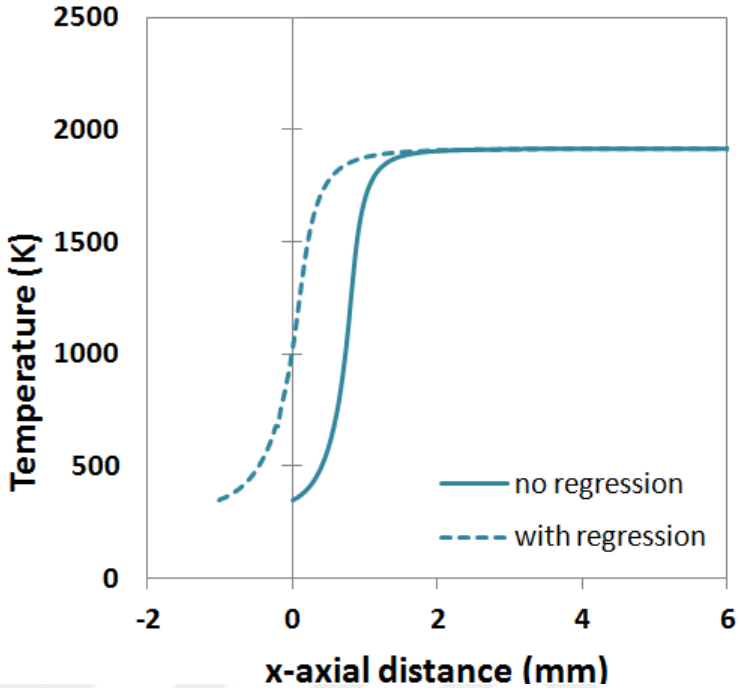

Figure 5.19 : Temperature profiles from the burning end with regression to x=1 mm corresponding t= 143ms and with no regression and for inlet temperature of 350 K.

Grid independency of the simulation is studied using various grid sizes. Figure 5.20 shows the temperature profiles both for no regression and 1 mm regression of the solid fuel boundary for grid sizes of 0.03 mm, 0.015 mm and 0.0075 mm with inlet temperature of 350 K. It is observed that, considered grid sizes result in the same temperature profiles for both models, no regression and with regression. Thus for computational cost, minimum grid size of 0.03 mm is used in the present study.

Temperature profile at a higher inlet temperature, 800 K, was also studied. As it is seen from Figure 5.21, introducing moving boundary does not affect the maximum temperature, in both (regression and no regression) models it reaches a maximum value of 2014 K. Compared to the temperature profiles with an inlet temperature of 350 K in figure 5.22, those obtained at 800 K show a steeper trend.

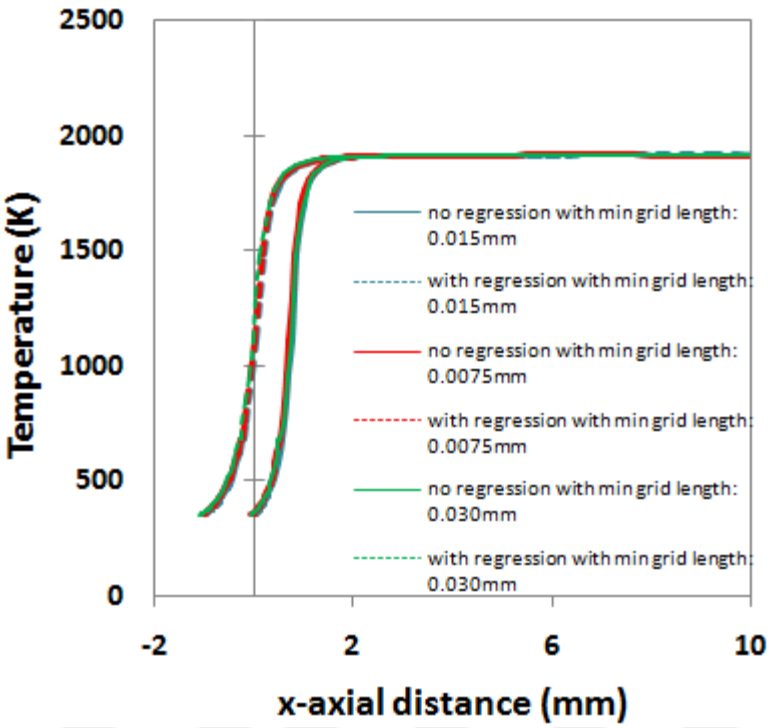

Figure 5.20 : Temperature profiles from the burning end with regression to x=1 mm corresponding t= 143ms and with no regression for minimum grid size of 0.03 mm, 0.015 mm and 0.0075 mm and for inlet temperature of 350 K.

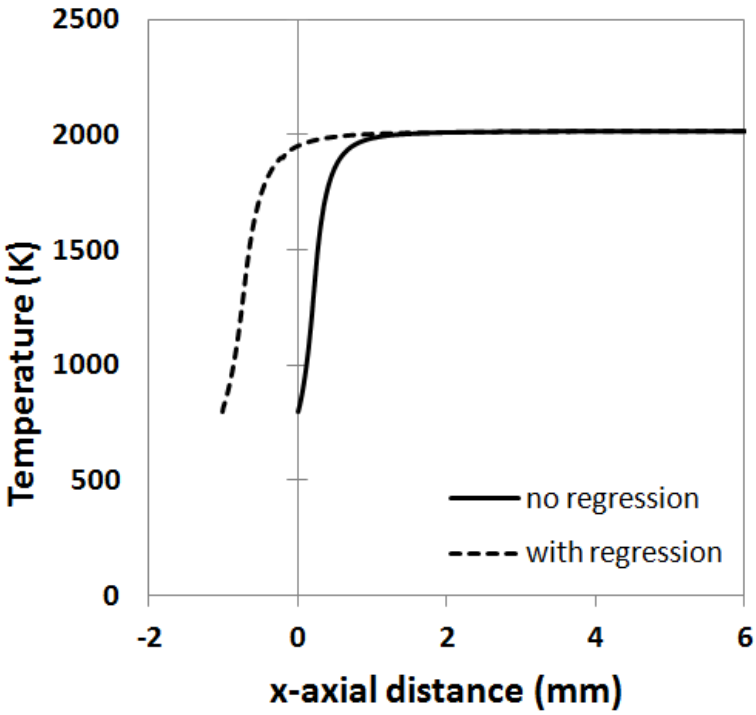

Figure 5.21 : Temperature profiles from the burning end with regression to x=1 mm corresponding t= 143ms and with no regression and for inlet temperature of 800 K.

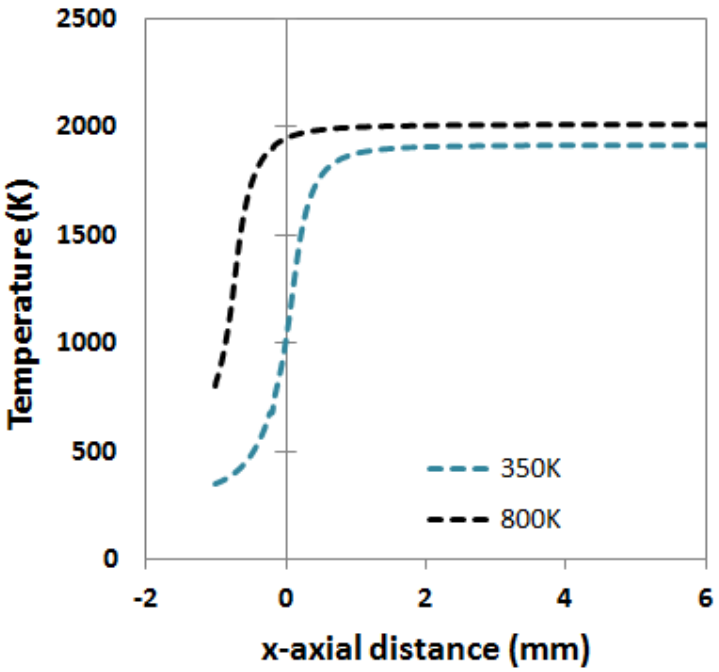

Figure 5.22 : Temperature profiles from the burning end with regression to x=1 mm corresponding t= 143ms and for inlet temperatures of 350 K and 800 K.

The comparison of temperature variations in the chamber for H_2 and C_3H_8 for the inlet temperature of 350 K at the same mass flux of 11.39 kg/m^{2}s is shown in figure 5.23. In the reaction zone, the temperature increases to 1918 K for the hydrogen combustion and to 1792 K for the propane combustion, respectively.

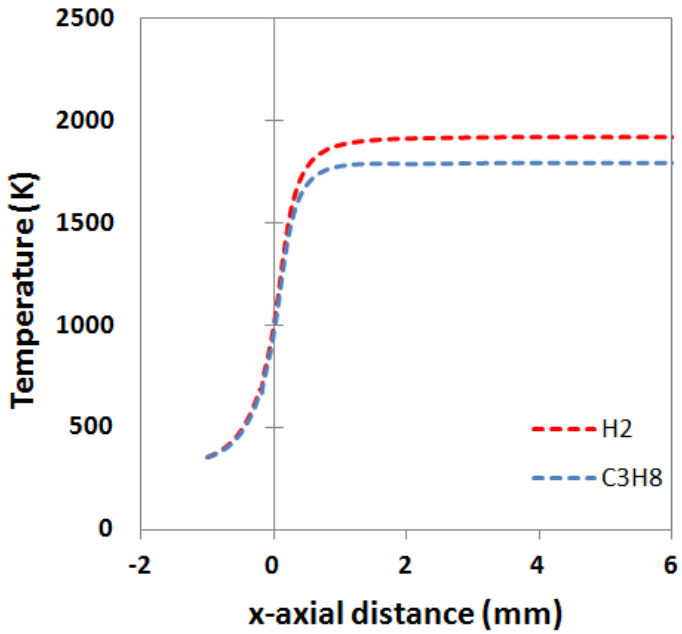

Figure 5.23 : Temperature profiles from the burning end with regression to x=1 mm corresponding t= 143ms for H_2 and C_3H_8 combustion.

The velocity distribution along the x-axis with inlet temperature of 350 K and equivalence ratio of 0.7 with regression and no regression is presented in figure 5.24. The temperature increases rapidly in the 2 mm thin reaction zone as shown in the previous figures. The mixture of combustion gases expands and the velocity of the gaseous mixture increases from 14.23 m/s to 77.76 m/s in this thin zone. The corresponding Mach number is 0.0386 for the inlet velocity and it reaches the value of 0.09 at the end of the reactive flame zone.

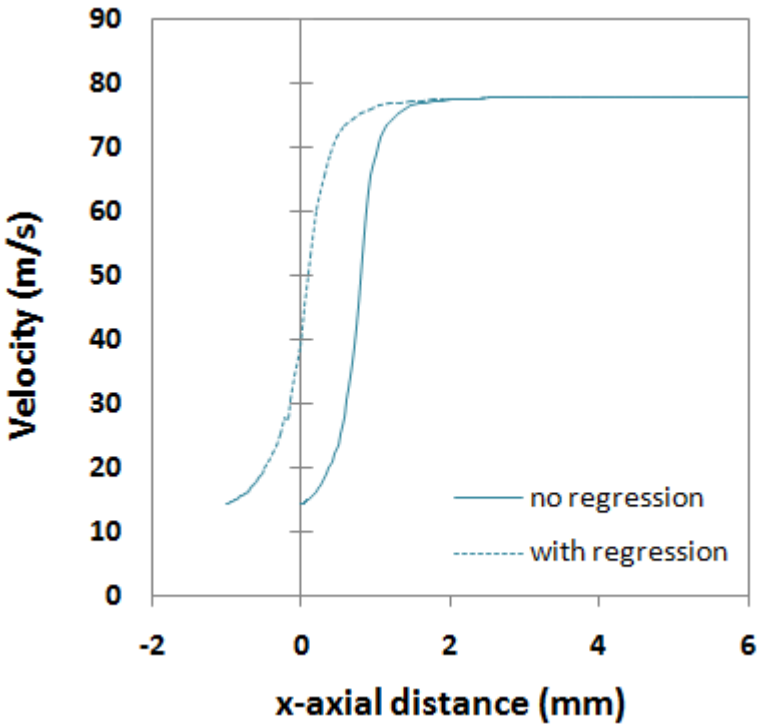

Figure 5.24 : Velocity of gas mixture versus distance from the burning end with regression to x=1 mm corresponding t=143ms and with no regression and for inlet temperature of 350 K.

5.3.1.1 Thrust curves

Effects of regressive boundary on SRM thrust curves are also investigated. Thrust is known as the force that propels SRM which is due to the effect of pressure exerted on the walls of the combustion chamber.

The pressure distribution within the combustion chamber is asymmetric, inside the chamber only minimal pressure variations are observed whereas on the downstream, near the nozzle, it decreases. The gas pressure on the downstream and the force associated with that is not compensated by the outside. As a result of the internal and

external pressure differences and pressure exerted on the walls of the chamber, thrust occurs and propels chamber forward.

Considering the forces due to the pressures exerted on the walls of the chamber by the combustion gases and the surrounding atmosphere and taking the cross sectional area of the exit on downstream and using that as the boundary between the inner and outer mathematically, thrust, F, is defined as:

$$F = \dot{m}V_e + (p_e - p_0)A_e \tag{5.2}$$

where $\dot{m}$ is the mass flow rate, V_e is the exit velocity of the gaseous mixture and p_e and p_0 are the exhaust gas pressure and ambient pressure, respectively. A_e is defined as the cross sectional area at the exit of at the nozzle. The first term on the right-hand side of the equation is the contribution due to flow and the second term on the right-hand side is called pressure thrust which could only have negative value or could be equal to zero for a nozzle with an optimum expansion ratio ($p_e = p_0$). Under the optimal design criteria, thrust achieves its highest value and thus SRM performance achieves its maximum level.

Within the explained lab-scale SRM model, as the gaseous combustion products leave the nozzle with a Mach number greater than 1 (at supersonic conditions) significant thrust occurs propelling the chamber forward. Figure 5.25 illustrates the time dependent thrust profiles that are obtained for hydrogen combustion model at varying inlet temperatures.

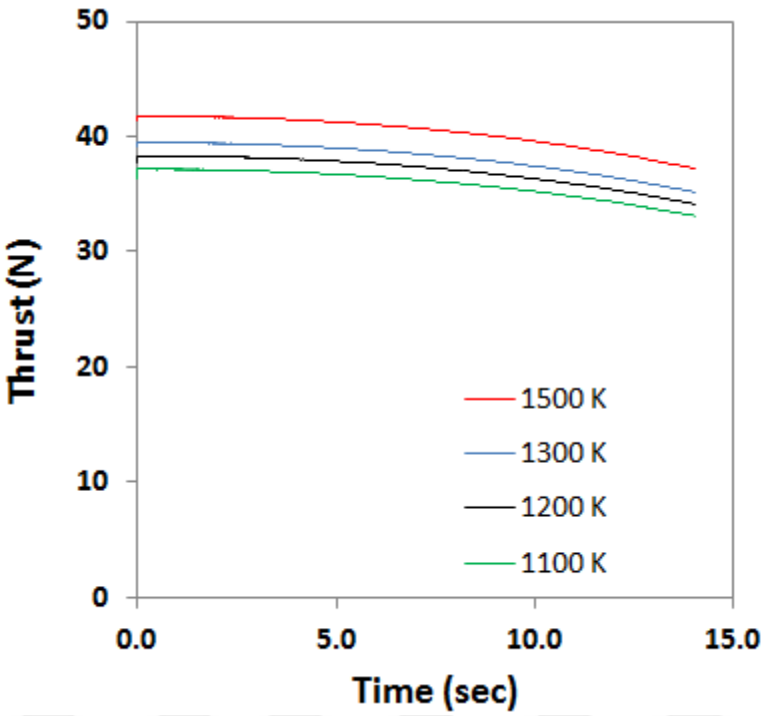

Figure 5.25 : Thrust profiles for H_2 combustion for various inlet temperatures.

In Figure 5.25, at each inlet temperature, the thrust curve starts from a particular value since the steady results are set as the initial conditions for regressive boundary unsteady model. Thrust profiles remain almost constant throughout the first second. After the first second, a gradual decrease starts in the thrust value. When the propellant is consumed totally, corresponding time t=14.35 seconds, the decrease in thrust is about 10 %. These trends can be explained by considering the regressive boundary. The lab scale motor chamber is 270 mm long including the nozzle. A solid fuel thickness of 100 mm is added to it. During the regression, the volume change of the chamber is about 44 %. The increase in the chamber volume results in pressure decrease. Thus, thrust decreases in time. Figure 5.25 also shows that increase in inlet temperature results in an increase in thrust. Similarly, thrust profiles for propane combustion model are provided for different inlet temperatures in figure 5.26.

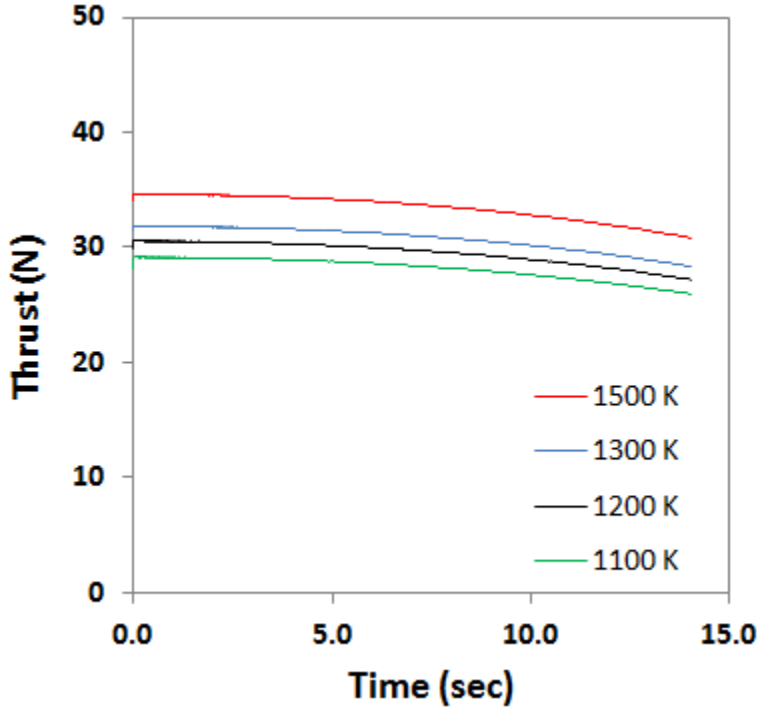

Figure 5.26 : Thrust profiles for C_3H_8 combustion for various inlet temperatures.

Increased inlet temperatures increase the thrust and the thrust versus time behaves as that for H_2 combustion.

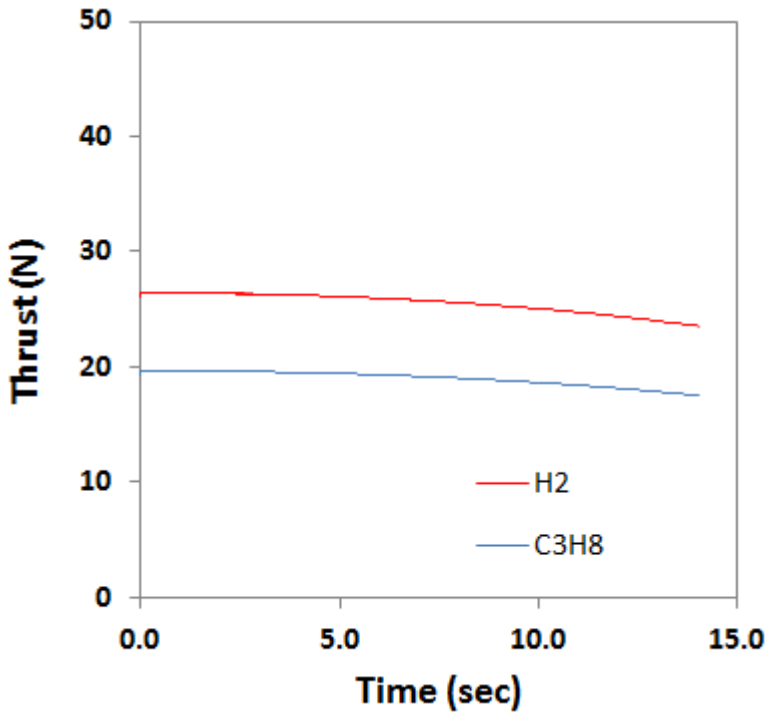

Figure 5.27 : Thrust profiles for H_2 and C_3H_8 combustion, inlet temperature of 350 K for mass flux of 11.39 kg/m^{2}s.

Hydrogen and propane combustion models are also compared for the inlet temperatures of 350 K and 800 K in Figures 5.27 and 5.28, respectively. For the inlet temperature of 350 K in figure 5.27, maximum thrust is 26.2 N for hydrogen combustion and 19.6 N for propane combustion, respectively. These values decrease to 23.1 N for hydrogen and 17.5 N for propane combustion when the solid propellant is entirely consumed at time t=14.35 seconds.

As seen in figure 5.28, maximum thrusts are 32.9 N and 24.7 for hydrogen and propane combustions with the inlet temperature of 800 K. These values decrease to 29.2 N and 22.8 N for hydrogen and propane combustions, respectively.

Figures 5.27 and 5.28 show that the thrust value of the hydrogen combustion model is higher than that of the propane combustion model for the same mass influx and the same inlet temperature on the head end burning regressive boundary.

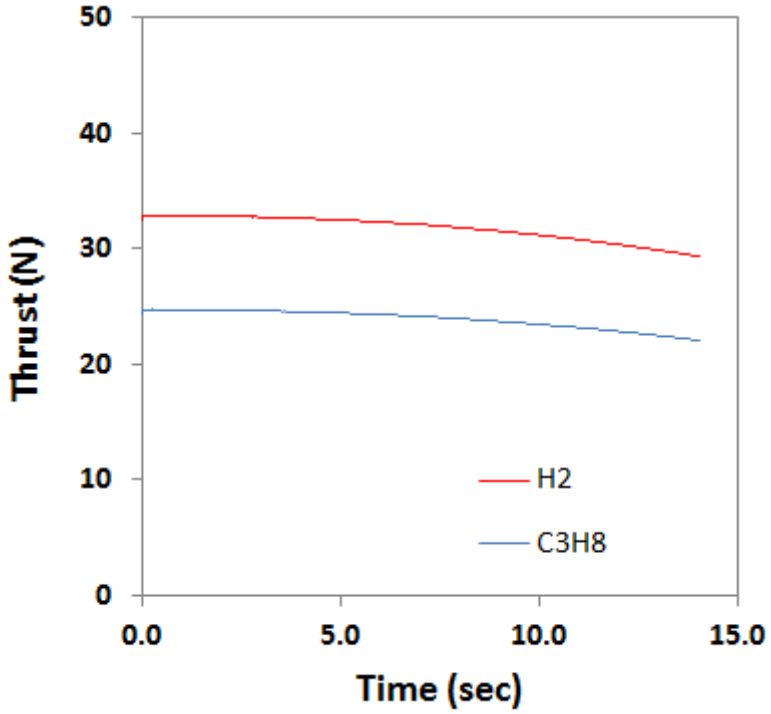

Figure 5.28 : Thrust profiles for H_2 and C_3H_8 combustion, inlet temperature of 800 K for mass flux of 11.39 kg/m^{2}s.

5.3.2 Pressure dependent regressive boundary model computations

In this final section, reacting flow with pressure dependent regressive boundary model is examined for different geometries, which are lab-scale motor [40] and Onerac 1 [20] geometry. Here, it is aimed to compare the constant burning rate and pressure dependent burning rate simulations in SRMs. The burning rate of the solid propellant, which depends on the chamber pressure, is taken as follows;

$$\dot{r_b} = \alpha p^n \tag{5.3}$$

For the test cases, different n values are performed in order to see their effects on both burning rate and pressure during the combustion process in the rocket.

5.3.2.1 Pressure dependent regressive rate model for lab-scale motor

Lab-Scale solid rocket motor was performed with non-regressive reactive model and a constant velocity regressive reactive model in the previous sections. In this part, the same geometry as that with pressure dependent burning rate is considered.

There are four boundary conditions representing this lab-scale model. The left end-burning part is taken as a subsonic inlet. The mass flux at this injecting boundary is calculated with respect to solid fuel regression rate as explained in Regression Model Section. The injection temperature is 350 K as in the study by Havlucu and Kirkkopru [61]. The fuel-air equivalence ratio is taken 0.7. The upper side has a symmetry boundary condition. The lower solid impermeable boundary and the nozzle wall are adiabatic. The gaseous mixture leaves the nozzle at supersonic conditions. For supersonic outflow, the flow properties are calculated from the interior points.

For the chemical model, two step hydrogen combustion and propane combustion models, which are introduced before, are performed. Same grid structure is used compared to previous lab-scale motor simulation. The commercial software ANSYS Fluent 15.0 [63] is used to solve the governing equations coupled with the chemical reactions. The combustion process is modeled using finite rate chemistry. Spatial discretization is achieved using second order upwind differencing scheme whereas first order implicit method is used for temporal discretization.

The convergence residuals for continuity, velocity, energy, and mass fractions of the species are set to be 10^{-3} for every iteration in each time step for time dependent calculations. When the steady state results are reached, the absolute residual of energy and velocity are $5x10^{-5}$ and $7x10^{-5}$, respectively.

As explained in Numerical Model section, "DEFINE_EXECUTE_AT_END" and "DEFINE_PROFILE" UDF's are added to the constant regression rate model. At the end of every time step, the UDF "DEFINE_EXECUTE_AT_END" is called in order to calculate the average pressure in the combustion chamber. Using the pressure dependent burning rate expression which is proposed by Vieille [65, 66], the burning rate of the solid fuel is calculated with the computed average pressure. Because the density of the propellant is known, the inlet gas mixture velocity on the burning boundary is calculated through the known burning rate (Equation 5.3). Then, the "DEFINE_PROFILE" UDF is called in order to update the velocity inlet at the solid fuel boundary. Eventually, the "DEFINE_GRID_MOTION" is called to degrade the regressing boundary according to the calculated burning rate within the time step. After all of these calculations have been performed, the solver continues to the next time step. This procedure is carried out until all the attached solid fuel is consumed.

At the end of every time step, new rectangular grids are added to the left of the computational domain for every regression distance of 0.03 mm using Dynamic Layering Method offered by ANSYS Fluent 15.0 [63]. The initial thickness of the propellant 100 mm is added to the chamber of total length of 270 mm. Depending on the burning rate, the propellant is consumed between the 11th and 14th seconds.

For the calculations with regressive propellant, time dependent equations for non-regressive boundary model with chemical reaction are solved until steady state is reached for the given inlet temperature. Steady state solution is achieved by setting the temperature at all grid points equal to the adiabatic flame temperature of the combustion model. Accordingly, the velocity field and species mass fractions in the domain are taken equal to the inlet velocity and species mass fractions at the end burning boundary. Then, these steady results are set as initial conditions for the unsteady simulation of reactive flows for pressure dependent burning rate with regressive boundary, as done by others [51, 61]. α is taken as 0.01 for all the pressure dependent unsteady calculations [60].

Different pressure indexes *n* are used to investigate its effect on burning rate and chamber pressure. Figure 5.29 compares the time dependent burning rates for n=0.2, 0.4 and 0.6 and constant burning rate. For n=0.2 the initial burning rate is the highest among the others, thus the solid fuel is consumed in a shorter time compared to n=0.4 and 0.6. For the three cases of n=0.2, 0.4 and 0.6 the solid fuel consumption times are 11.19 s, 12.53 s and 14 s, respectively. As combustion process continues the burning rates for all cases decrease in time, since the chamber pressure decreases as the chamber volume increases.

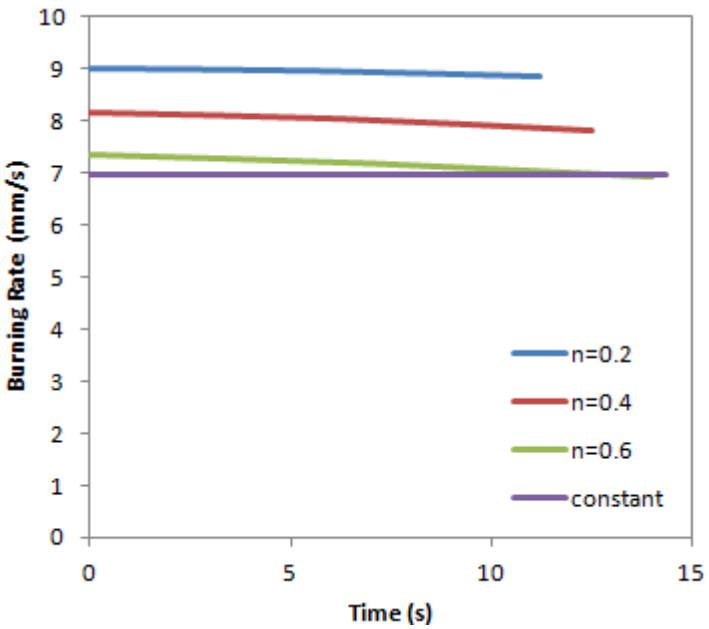

Figure 5.29 : Comparison of burning rates for n values of 0.2, 0.4 and 0.6, where α=0.01 and for constant burning rate.

In figure 5.30, the chamber pressure change in time is shown both for constant burning rate and pressure dependent burning rate for n values of 0.2, 0.4 and 0.6. The initial pressure in the chamber is 0.6 MPa for all the simulations, a result from non-regressive steady state calculation. The pressure decreases 5% in the constant burning rate process due to the volume increase in geometry. However, the pressure decreases about 10% in the pressure dependent burning rate simulations. Because the burning rate depends on decreasing pressure leading to decreasing inlet mass velocity, this cycle induces faster pressure decrement in time compared to that for constant burning rate.

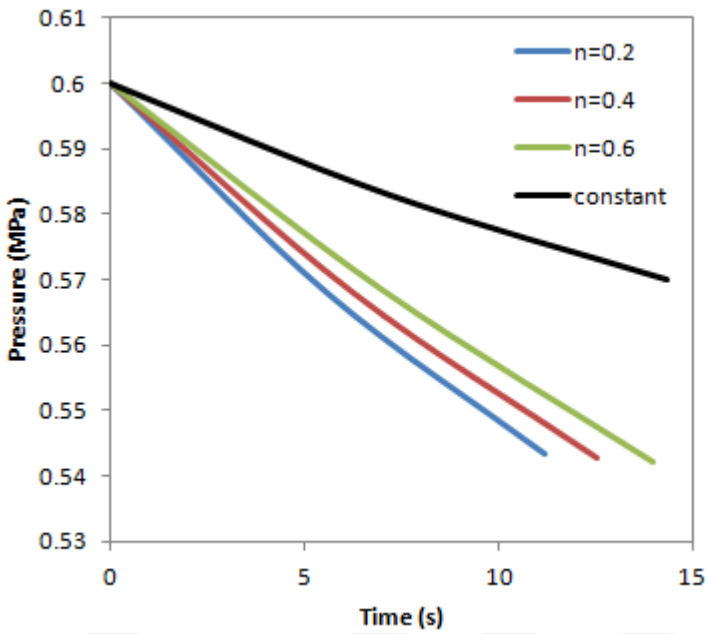

Figure 5.30 : Variation of chamber pressure with time for n values of 0.2, 0.4 and 0.6, where α=0.01 and for constant burning rate.

Within the very thin flame zone close to solid propellant surface, the spatial variations of temperature and species mass fractions are very rapid as depicted in Figure 5.31. The temperature increases from the feeding boundary temperature 350 K to 1902 K in a two millimeter distance. The flow characteristics within this region are captured using grids that are highly clustered near the head-end burning part of the motor. Figure 5.31 also compares mass fractions of H_2, O_2 and H_2O species along the axis of the combustion chamber. H_2 and O_2 mass fractions decrease from 0.0183 and 0.21 to 0 and 0.0636, respectively. The mass fraction of the product, H_2O, increases from 0 to 0.1647.

Grid independency study is performed using various grid sizes. Figure 5.32 shows the temperature profiles both for constant burning rate and pressure dependent burning rate for minimum grid sizes of 0.03 mm, 0.015 mm and 0.0075 mm with inlet temperature of 350 K at the time when all the solid fuel is consumed. It is observed that, considered grid sizes result in the same temperature profiles for both burning rate models. Thus for computational cost, minimum grid size of 0.03 mm is used in the present study.

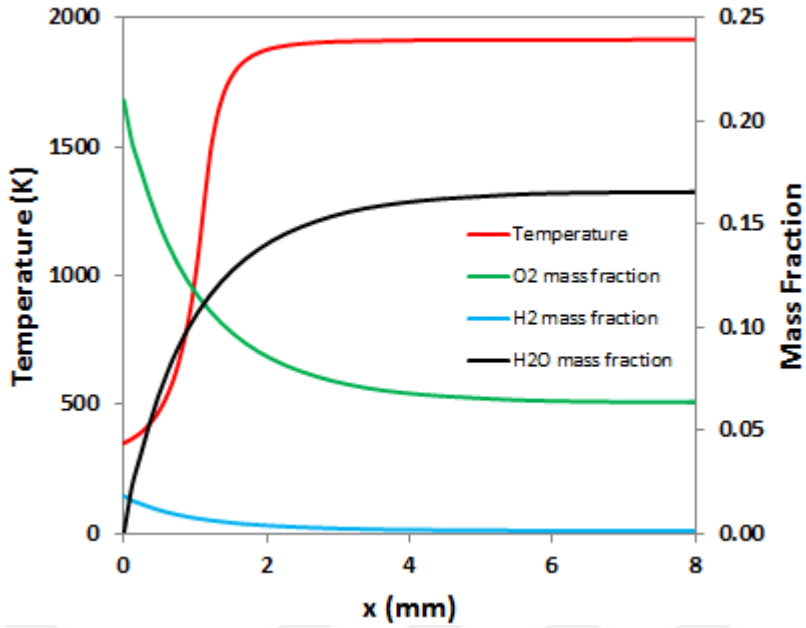

Figure 5.31 : Spatial Variations of temperature and mass fractions along x-axis from the burning end with pressure dependent burning rate when all the solid fuel is consumed at t=14 s., when n=0.6 and α=0.01

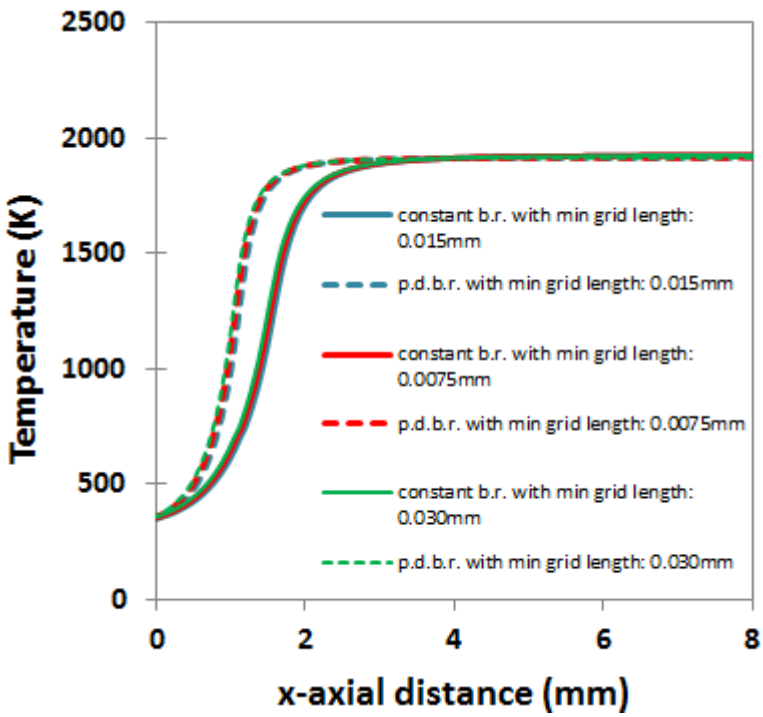

Figure 5.32 : Temperature profiles from the burning end at the time when all the solid fuel is consumed with constant burning rate at t=14.35 s and pressure dependent burning rate at t=14 s, n=0.6 and α=0.01 for minimum grid sizes of 0.03 mm, 0.015 mm and 0.0075 mm when inlet temperature is 350 K.

Figure 5.33 illustrates temperature profiles for both constant and pressure dependent burning rate regression of the solid fuel boundary with inlet temperature of 350 K. Considering an equivalence ratio of 0.7 for H_2 combustion, the temperature reaches a maximum value of 1918 K in constant burning rate and 1902 K in pressure dependent burning rate indicating that the maximum temperature is affected slightly by the pressure dependency of burning rate.

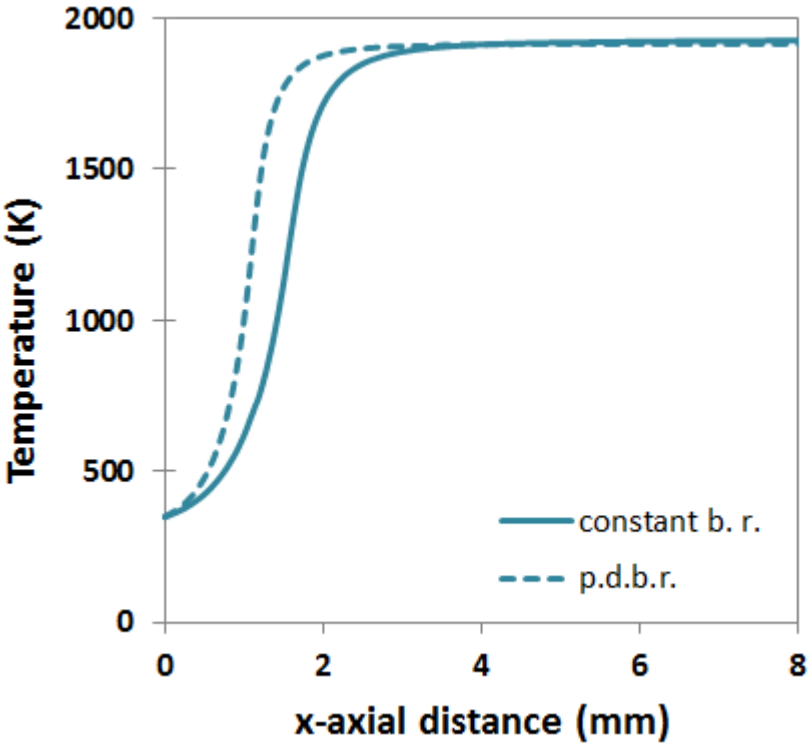

Figure 5.33 : Temperature profiles from the burning end when all the solid fuel is consumed with constant burning rate at t=14.35 s and pressure dependent burning rate at t=14 s when n=0.6 and α=0.01 for inlet temperature of 350 K.

Spatial temperature profiles for inlet temperatures of 350 K and 800 K for H_2 combustion are shown in Figure 5.34. Temperature profile for inlet temperature of 800 K has a steeper spatial gradient than that for inlet temperature of 350 K, leading to a higher maximum gas mixture temperature of 2001 K compared to 1902 K for inlet temperature of 350 K.

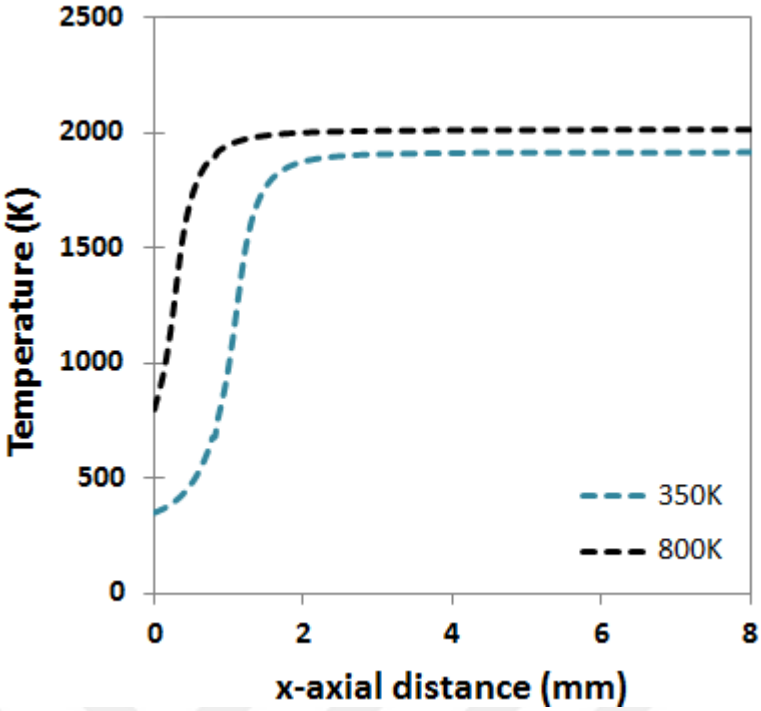

Figure 5.34 : Temperature profiles from the burning end with pressure dependent burning rate when all the solid fuel is consumed corresponding t=14 s and n=0.6, α=0.01 for inlet temperatures of 350 K and 800 K.

Spatial temperature variations for H_2 and C_3H_8 in the chamber for the inlet temperature of 350 K are compared in Figure 5.35. In the reaction zone, the temperature increases to 1902 K for the hydrogen combustion and to 1775 K for the propane combustion, respectively. These values were 1918 K and 1792 K for constant burning rate in the study of Havlucu and Kirkkopru [61], respectively. For both constant and pressure dependent burning rate the maximum temperature is achieved in the H_2 combustion, for the parameters under consideration.

The axial velocity distribution along the x-axis corresponding to inlet temperature of 350 K for both constant rate regression and pressure dependent regression is presented in Figure 5.36. The temperature of the gas mixture rises rapidly in the 2 mm thin reaction zone as shown in the previous figures. In this region, the mixture of combustion gases expands and the velocity of the gaseous mixture increases from 13.39 m/s to 74.26 m/s in the pressure dependent burning rate simulation and from 14.23 m/s to 77.76 m/s in the constant burning rate model in the study of Havlucu and Kirkkopru [61]. The flow inlet Mach number is 0.0363 and the flow Mach number reaches the value of 0.0859 towards the end of the reactive flame zone for the pressure dependent regression model, which is slightly lower than the value

obtained in the unsteady burning rate calculations [61]. This is due to decreasing pressure dependent burning rate with decreasing pressure in the chamber with increasing chamber volume.

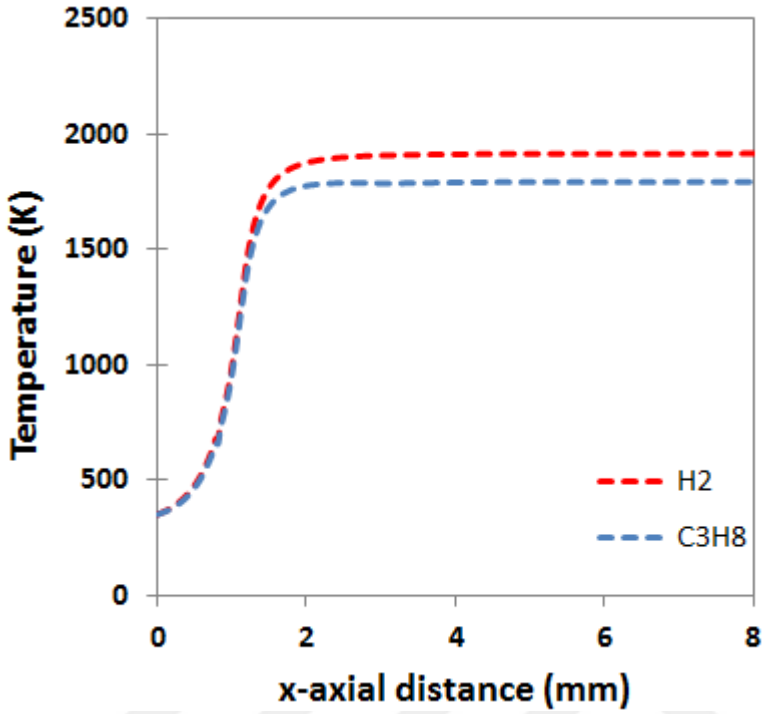

Figure 5.35 : Temperature profiles from the burning end with pressure dependent burning rate when all the solid fuel is consumed at t=14 s, n=0.6 and α=0.01 for H_2 and C_3H_8 combustion.

Figure 5.37 illustrates the density variation of the gas mixture both for constant and pressure dependent simulations when all the solid fuel is consumed. The density decreases from 0.850 kg/m^3 to 0.153 kg/m^3 for the pressure dependent model and from 0.8 kg/m^3 to 0.146 kg/m^3 for the constant burning rate model, respectively.

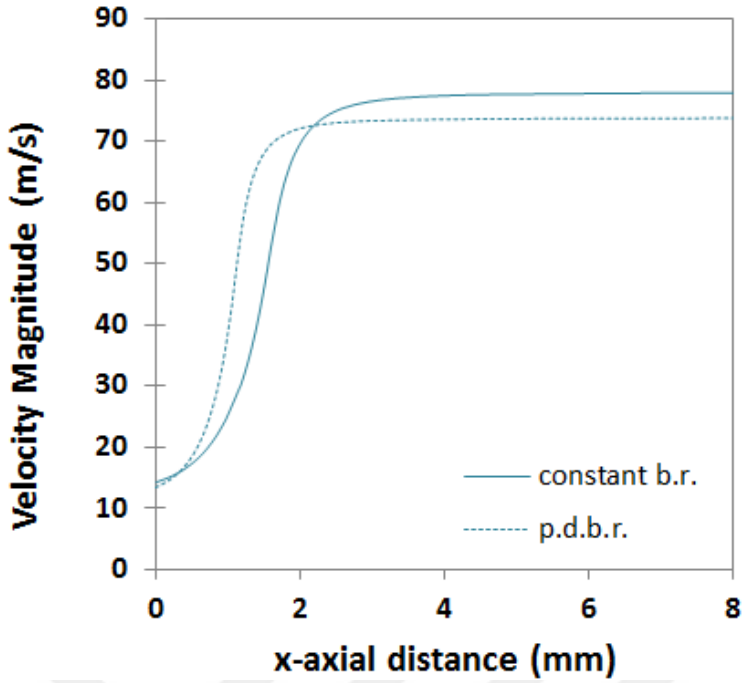

Figure 5.36 : Axial variation of velocity of gas mixture from the burning end when all the solid fuel is consumed at t=14.35 s for constant burning rate and t=14 s, n=0.6 and α=0.01 for pressure dependent burning rate for inlet temperature of 350 K.

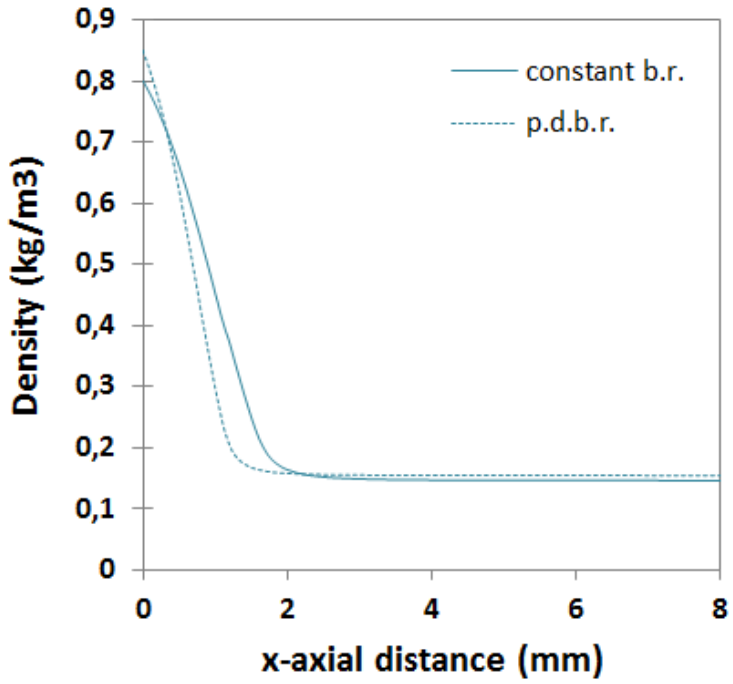

Figure 5.37 : Density variation of gas mixture with distance from the burning end when all the solid fuel is consumed at t=14.35 s for constant burning rate and t=14 s, n=0.6 and α=0.01 for pressure dependent burning rate for inlet temperature of 350 K.

5.3.2.2 Pressure dependent regressive rate model for Onerac 1 motor

Similar to pressure dependent burning rate model with reactive flow in lab-scale motor, non-regressive model and a constant velocity regressive model were introduced in the previous sections for Onerac 1 Motor. Here, the same geometry is considered and pressure dependent regression rate with reactive flow is taken into account.

328 x 32 grids are used in the cold flow simulation with stagnant injecting wall for the computational domain of Onerac 1. For this reacting flow case with pressure dependent regressive boundary, temperature, species mass fractions, velocity and density of the gas mixture vary very rapidly within a very thin zone adjacent to the regressive burning boundary. To better capture these rapid variations of flow properties within this thin regime, cells were highly clustered in the neighborhood of the head end burning part of the motor. However, Onerac 1 geometry is not suitable for the simulation of regressing boundary using rectangular grids. Therefore, triangular cells are used. Figure 5.38 demonstrates a part of the computational grids near the burning boundary of the solid rocket motor. The triangles next to the transpiring side-wall are equilateral. The length of one side of the triangle is taken as 0.01 mm, 0.02 mm and 0.03 mm. 41 million triangular cells are used in the computational domain for the grid length size of 0.03 mm. Boundary conditions are treated as the same as those previous regressive boundary model computations of Onerac 1 case. Propane combustion is used for the reactive model.

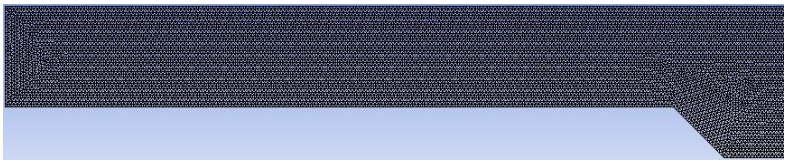

Figure 5.38 : Grid structure from to the burning boundary for Onerac 1.

The combustion model is considered using finite rate chemistry. First order implicit method is employed for temporal discretization. Spatial discretization is performed using second order upwind differencing scheme. Under-relaxation factor of 0.65 within each time step is used for pressure, momentum and temperature for numerical stability.

In order to start the solution for the pressure dependent regressive rate model, first steady state solution is obtained by using time marching technique with the initial

condition where the adiabatic flame temperature is set at all grid points. These steady results are set as initial conditions for the reactive flow simulation with unsteady pressure dependent burning rate on the regressive boundary, as done by others [51]. Inlet temperature of 350 K with equivalence ratio of 0.95 is considered. The burning rate is calculated via Robert Vielle's equation as explained in regressive boundary model in Section 3. For the simulations, the burn rate coefficient α is taken as 0.01. Various pressure indexes *n* are performed to investigate its effect on the burning rate and chamber pressure.

Figure 5.39 shows the time dependent pressures for n=0.2, 0.4 and 0.6 and constant burning rate. They all start from the same initial pressure which is 465 kPa, since the initial conditions are same for the unsteady simulations. For the constant burning rate, the pressure decreases 6 % until the solid fuel finishes. However, for the pressure dependent burning rate, the chamber pressure decreases more compared to constant burning rate. As the pressure index increases from 0.2 to 0.6, the pressure decrease increases. The pressure decreases from 465 kPa to 403 kPa in 1.77 seconds for n=0.2, which corresponds to 13.3 % change. This pressure decline is 17.2 % and 18.9 % for n=0.4 and n=0.6, respectively. Solid fuel consumption durations are 2.11 seconds and 2.52 seconds for n=0.4 and n=0.6, respectively.

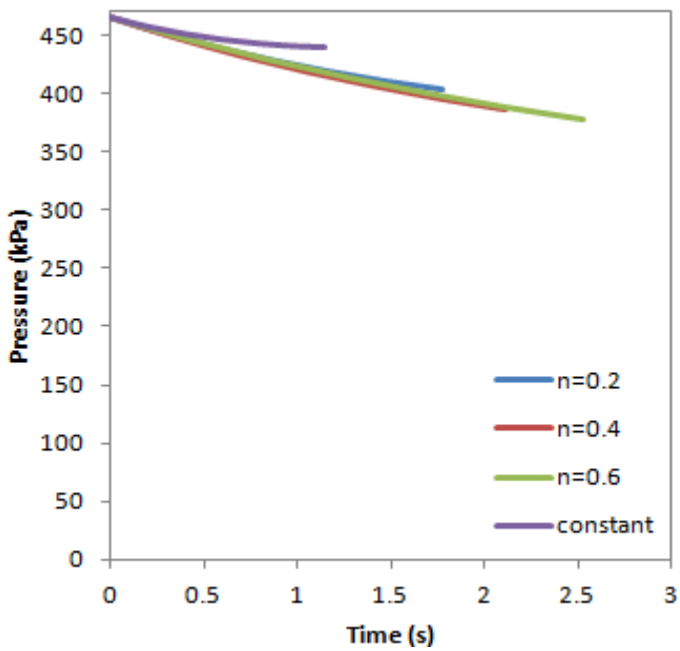

Figure 5.39 : Variation of chamber pressure for n values of 0.2, 0.4 and 0.6, for α=0.01 and constant burning rate.

Figure 5.40 shows the time dependent burning rates for pressure indexes n=0.2, 0.4 and 0.6 and for constant burning rate. The constant burning rate is 13 mm/s. The burning rate starts from 8.58 mm/s and decreases to 8.34 mm/s for n=0.2. Similarly, the burning rate diminishes from 7.36 mm/s and 6.31 mm/s to 6.83 mm/s and 5.57 mm/s for n=0.4 and 0.6, respectively. The decrease in burning rate for n=0.2, 0.4 and 0.6 are 2.7 %, 7.2 % and 11.7 % respectively. Increasing the pressure index increases the pressure change as well. Finally, as the burning rate decreases, consumption time of the solid fuel increases.

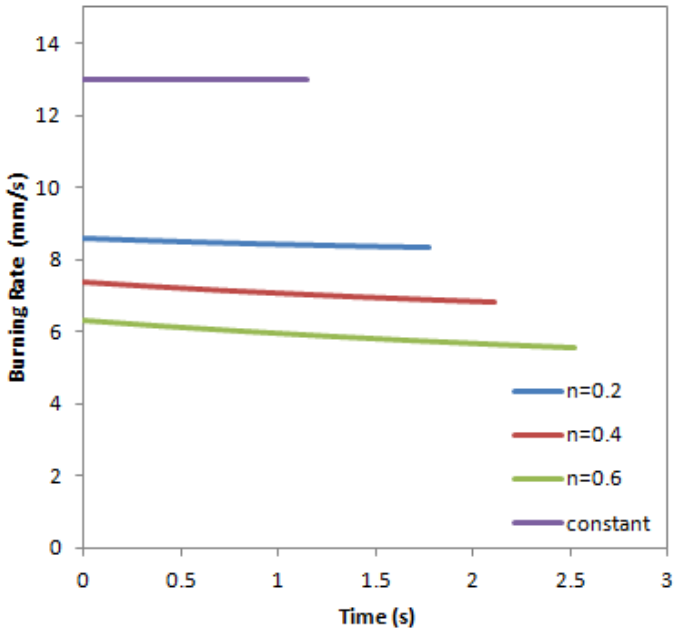

Figure 5.40 : Comparison of burning rates for n values of 0.2, 0.4 and 0.6, when α=0.01 and constant burning rate.

The initial burning rate is the highest for n=0.2 among the others. As combustion process takes place, the burning rates for all cases decrease in time since the chamber pressure decreases.

Figure 5.41 shows the velocity variation of the gaseous mixture in the y direction 100 mm ahead from head-end wall when all the solid propellant is consumed. The inlet velocity of the gas mixture starts with 19.9 m/s on the boundary and in a few millimeters in the flame zone it reaches peak value of 51.8 m/s where the temperature takes its maximum value. After this zone, the velocity decreases fast to zero at the symmetry boundary which is consistent with the symmetry boundary condition.

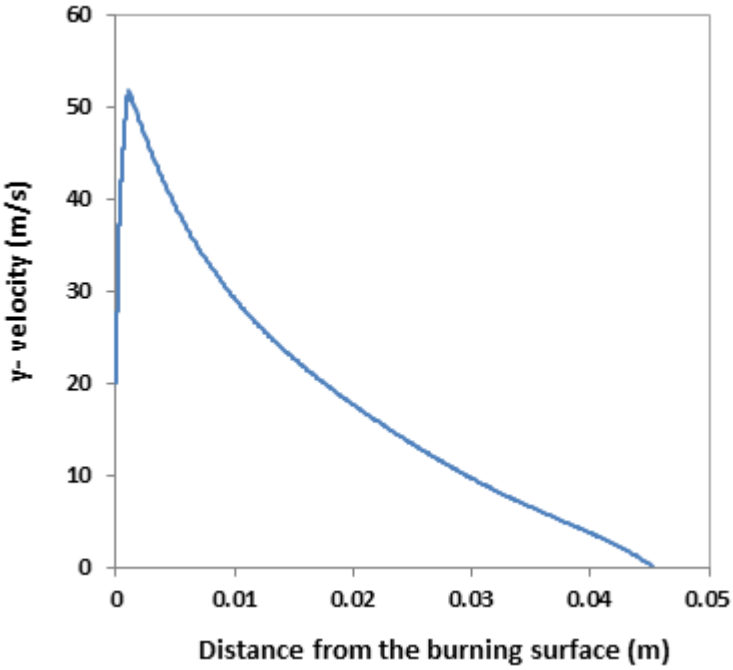

Figure 5.41 : Y-Velocity variation from the burning surface when all the solid fuel is consumed at t=2.52 s. when n=0.6 and α=0.01 for inlet temperature of 350 K.

The variations of x-velocity with y direction at axial locations 66 mm, 133 mm and 200 mm from head-end wall are presented in Figure 5.42. Here, the inlet temperature is 350 K and equivalence ratio is 0.95. At the burning surface the x-velocity is zero. For all the three locations the velocity of the gas mixture increases to 101 m/s, 212 m/s and 327 m/s at the centerline of the chamber, respectively.

Figure 5.43 illustrates the velocity magnitude for the locations as in the Figure 5.42. The velocity magnitude is 19.9 m/s on the burning surface and since the y-velocity is zero on the symmetry boundary, the velocity magnitudes are identical compared to x-velocities at the corresponding locations, which are 101 m/s, 212 m/s and 327 m/s, respectively. This indicates that the velocity magnitude is controlled by x-velocity. The corresponding flow Mach number is 0.053 for the inlet velocity and it reaches the value of 0.118 at the end of the reactive flame zone for the pressure dependent model. As the flow targets to the nozzle, the flow Mach number increases and reaches to 1.0 at the throat of the nozzle. Its value is 1.56 at the exit.

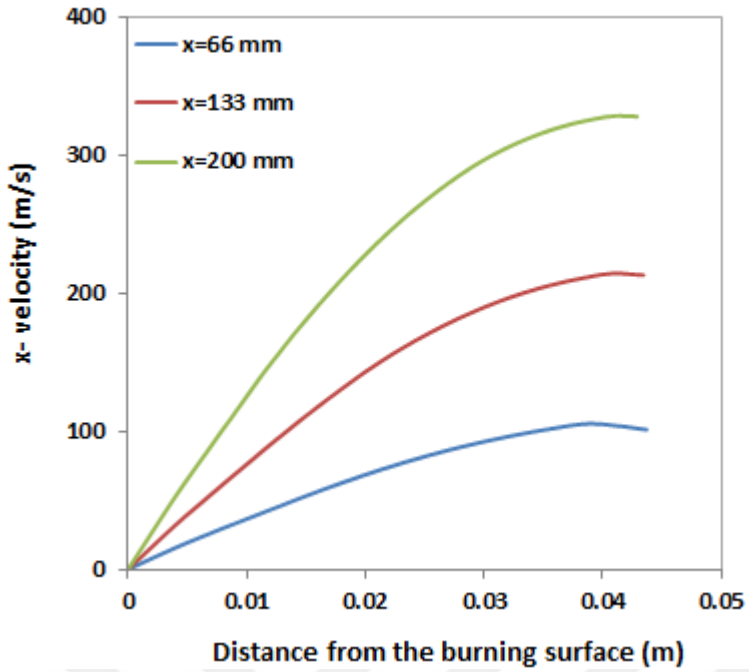

Figure 5.42 : X-Velocity variations from the burning surface at the locations of x=66 mm, 133 mm and 200 mm when all the solid fuel is consumed at t=2.52 s. when n=0.6 and α=0.01 for inlet temperature of 350 K.

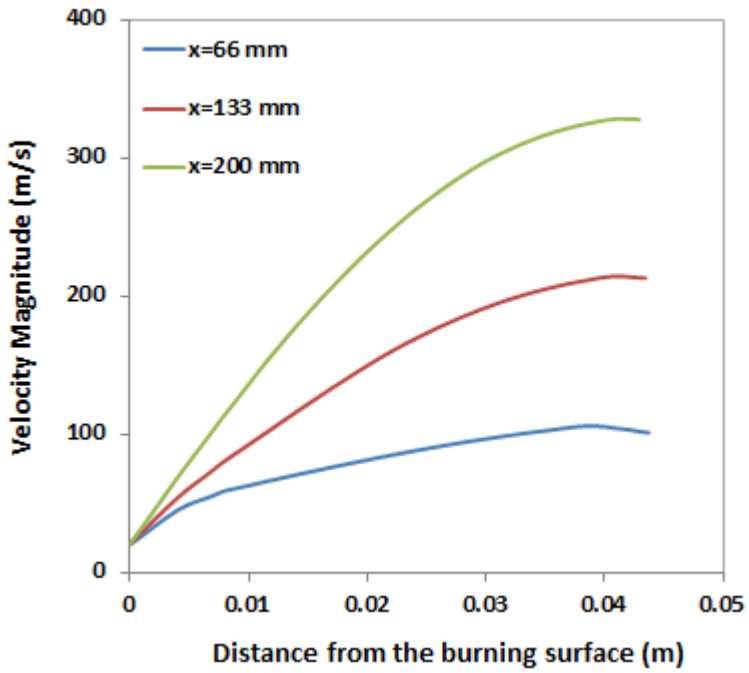

Figure 5.43 : Velocity magnitude from the burning surface at the locations of x=66 mm, 133 mm and 200 mm when all the solid fuel is consumed at t=2.52 s. when n=0.6 and α=0.01 for inlet temperature of 350 K.

The chemical reaction of the fuel air mixture in a very thin flame zone close to solid propellant surface is shown in Figure 5.44. Within this flame zone, the variations of flow properties such as temperature and species mass fractions are very rapid as illustrated before. The temperature increases from the feeding boundary temperature of 350 K corresponding the equivalence ratio 0.95 to 2197 K in a less than two millimeter distance. The flow characteristics within this region are captured using grids that are highly clustered near the regressing boundary. Figure 5.44 also illustrates mass fractions of C_3H_8, O_2, H_2O and CO_2 species along the axis of the combustion chamber. C_3H_8 and O_2 mass fractions decrease from 0.0548 and 0.21 to 0 and 0.011, respectively. The mass fraction of the products, H_2O and CO_2, increases from 0 to 0.0896 and 0 to 0.1644, respectively.

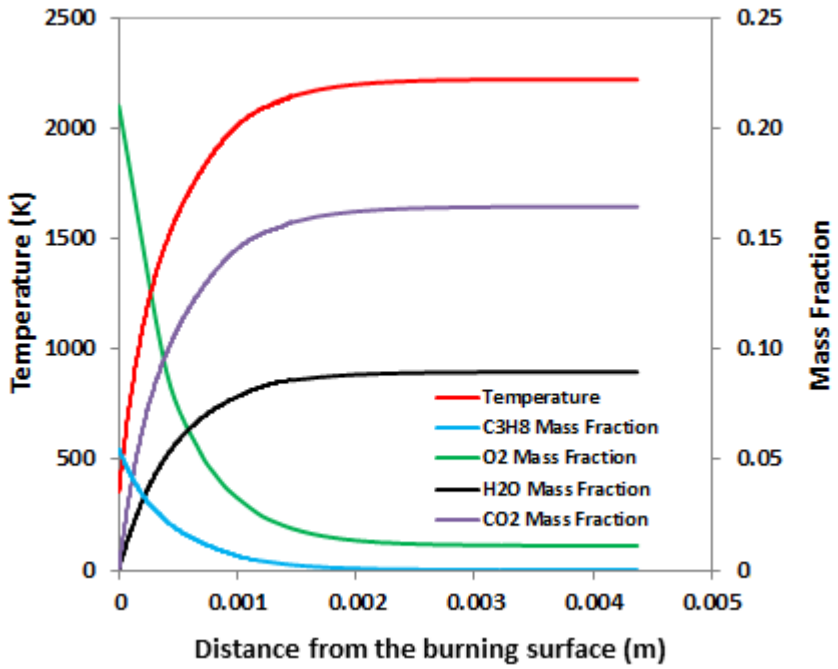

Figure 5.44 : Spatial variations of temperature and mass fractions along y-axis from the burning surface at x= 66 mm from the head end when all the solid fuel is consumed at t=2.52 s. when n=0.6 and α=0.01 for inlet temperature of 350 K. The centerline is 0.045 m away from the burning surface.

Grid independency is accomplished for different grid sizes. Figure 5.45 shows the temperature profiles for constant pressure dependent burning rate for triangular grid sizes of 0.01 mm, 0.02 mm and 0.03 mm with inlet temperature of 350 K at the time when all the solid fuel is consumed. It is observed that, considered grid sizes result in the same temperature profiles. Therefore, 0.03 mm thick grid size is used for the minimum grid.

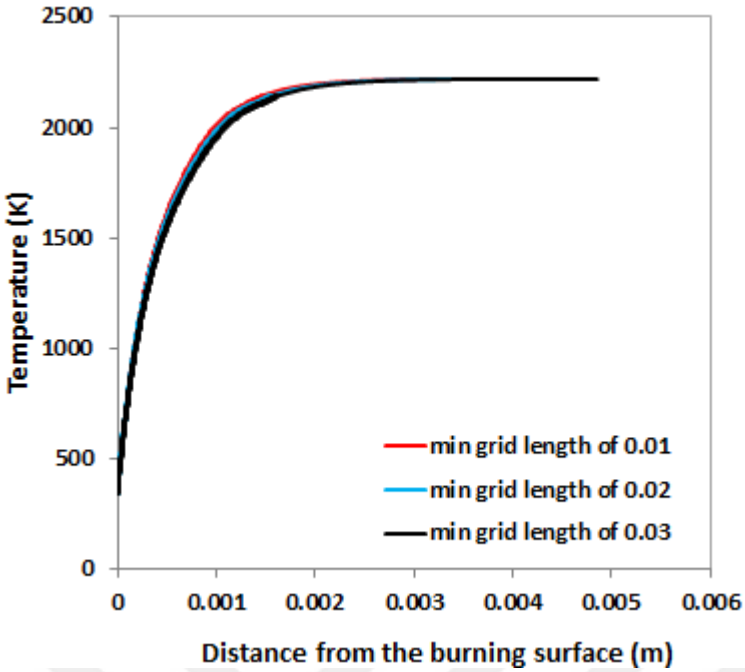

Figure 5.45 : Temperature profiles from the burning end at the time when all the solid fuel is consumed when all the solid fuel is consumed at t=2.52 s for minimum grid lengths of 0.01 mm, 0.02 mm and 0.03 mm. Here, n=0.6 and α=0.01 for inlet temperature of 350 K.

6. CONCLUSIONS

In this study, a computational model has been developed for the simulation of reactive fluid flow in a solid rocket motor (SRM) chamber involving variable internal geometry due to pressure dependent propellant burning surface regression. Complete conservation equations of mass, momentum, energy and species are solved with finite rate chemistry. The species are treated as thermally perfect. The model solves for a wide range of flow Mach number, from low speed subsonic inlet on the burning boundary to supersonic outlet at the exit of the nozzle. Spatial discretization is obtained using second order upwind differencing scheme and temporal discretization is achieved using first order implicit method. Stiff chemistry solver is used to avoid the stiffness problem due to the high temperature gradients as well as the species mass fraction gradients. Cells are highly clustered in the neighborhood of the end burning part of the motor to better capture these rapid variations of flow properties within the flame zone. The pressure and time dependent dynamic boundary is established on the burning regressive boundary. The regressive boundary, which results in increase in the volume of the combustion chamber with time, is treated by use of remeshing techniques. To do this, pressure dependent regression rate of the burning boundary is calculated, and at the end of every time step, the new location of the moving boundary is calculated and updated using the UDF's implemented in ANSYS Fluent 15 [63]. These UDF's are customized in C++ [67].

The developed model has been tested for four different cases available in the literature. Two cases are for cold flow, one of which is with a non-regressive boundary, however the other one is with regressive boundary. The other two cases are reacting flow with non-regressive boundaries. In the first test case, Onerac 1 geometry steady flow conditions are verified by using time marching method. Computed pressure, Mach number and streamline contours are compared well with the data in two different studies available in the literature. In the second case, the same Onerac 1 geometry with time dependent constant regression rate including cold

flow is considered. The streamline contours at five different times are compared with the available data. In addition to this, the time history of the head-end pressure is computed. Good agreement has been obtained with the study in the literature. In this case, injecting flow on the boundary is subsonic and it reaches supersonic flow conditions at the exit of the nozzle. Third case is a reacting flow in a 2-D rectangular channel with non-regressive side-wall mass injection without nozzle. The chemical model is propane combustion. The converged steady flow Mach number and chamber pressure are compared. Temperature and heat of reaction variations are computed within 2 mm region from the injecting boundary. The results show excellent agreement with the data in the literature. Finally, the last test case includes inviscid laminar reacting flow simulation in a two dimensional duct, which is a lab-scale motor. The chemical model is hydrogen combustion. Temperature and flow Mach number contours are computed and compared with the numerical study in the literature. Good agreement has been obtained. In this case, a wide range of flow Mach numbers from low to high exists in the flow field.

Time dependent cold and reactive flows were simulated successfully. Cold flow both with non-regressive and regressive boundary calculations agree with the numerical solutions in the literature. Reacting flow with stagnant wall simulation agreed for two different geometry models available in the literature. These results show that, the current simulation model is accurately developed.

Grid independency and accuracy are tested for the temperature variation in both constant regression and pressure dependent regression model with reactive flow in the lab-scale motor and in the pressure dependent regression model with reactive flow in Onerac 1 test case. It is concluded that fine grid, where flow variables have large gradients, is essential to capture the flow properties such as temperature variation. The computing time requirement for fine grid model is for sure greater than the coarse grid model.

Specific to this thesis study, constant and pressure dependent regressive boundary with reactive flow are modeled. To do this, firstly cold flow simulation with stagnant mass-added wall is developed. Then chemical kinetics are added to ANSYS Fluent 15.0 [63] to solve for reacting flow with stationary injecting wall. UDF (DEFINE_GRID_MOTION) is generated in C++ [67] and implemented in ANSYS Fluent 15.0 to move the regressive boundary with constant rate. Additional UDF's

(DEFINE_EXECUTE_AT_END and DEFINE_PROFILE) are developed to calculate the regression rate according to chamber pressure.

Hydrogen and propane combustion processes and thrust variations in time are examined for the constant rate boundary regression in the lab-scale model. Time dependent pressure and burning rate changes are illustrated in the pressure dependent burning rate simulation. Temperature and species mass fraction variations are given within the flame zone. Temperature, velocity and density distributions are compared for both constant burning rate and pressure dependent burning rate simulations for different geometries. Inlet temperature effect is given for both lab-scale model and Onerac 1 case. In Onerac 1 case, the reactive flow with pressure dependent burning rate is well simulated. The time history for chamber pressure and burning rate are investigated. The y-velocity variation from the burning surface, x-velocity variations from the burning surface at different locations and velocity magnitude variations at different locations are investigated in detail and thus the flow-combustion interaction is modeled in an accomplished way. The results indicate that the maximum temperature is not affected from the constant and pressure dependent regression rate. When compared constant and pressure dependent burning rate models, the pressure decrease is more in the pressure dependent model. The developed model is satisfactory to predict the reactive fluid flow features in a solid rocket motor (SRM) chamber with variable internal geometry due to the pressure dependent propellant burning surface regression using remeshing technic.

For future work, 3-D work with turbulence effect should be considered to reveal more realistic results. For the present laminar case, the chemical rates are based on Arrhenius chemical rate expressions, however turbulent fluctuation effects have not been considered. In addition to that, solid rocket motors generally contain double-base or composite propellants. A chemical model with detailed chemistry for such propellants need computational cost, however the model will be more realistic. Since the temperature of the combustion products are high, radiative heat transfer to the walls may be considered. In the present study, the burning rate is calculated from the chamber pressure. There are other parameters which affect the burning rate. As an example, the burning rate can be considered as a function of the initial temperature or composition of the solid propellant as a future work.

REFERENCES

[1] **Willcox, M. A., Brewster, M. Q., Tang, K. C., Stewart, D. S., and Kuznetsov, I.** (2007). Solid Rocket Motor Internal Ballistics Simulation Using Three-Dimensional Grain Burnback, *Journal of Propulsion and Power*, *23*, (3), 575–584.

[2] **Taylor, G. I.** (1956). Fluid Flow Regions Bounded by Porous Surfaces, *Proceedings of the Royal Society of London*, Series 234A, *1199*, 456-475.

[3] **Culick, F. E. C.** (1966). Rotational Axisymmetric Mean Flow and Damping of Acoustic Waves in a Solid Propellant Rocket, *AIAA Journal*, *4*, 1462-1464.

[4] **Harry, D.P.** (1977). Status of Nozzless Solid Rocket Motor Internal Ballistics Analysis, *AIAA Paper 77-910*, July.

[5] **Procinsky, I.M., and Yezzi, C.A.** (1982). Nozzless Performance Program, *AIAA Paper 82-1198*, June.

[6] **Olson, R.M., and Eckert, E.R.** (1966). Experimental Studies of Turbulent Flow in a Porous Circular Tube with Uniform Fluid Injection Through the Tube Wall, *Journal of Applied Mechanics*, *33*, 4, 950-953, December.

[7] **Yamada, K., Goto, M., and Ishikawa, N.** (1976). Simulative Study on the Erosive Burning of Solid Rocket Motors, *AIAA Journal*, *14*, 1170-1176, September.

[8] **Yagodkin, V.I.** (1967). Use of Channels with Porous Walls Studying Flows which Occur During Combustion of Solid Propellants, *Translated from Proceedings of the 18th Astronautics Congress*, 3, 69-79.

[9] **Yuan, S.W., and Finkelstein, A.B.** (1956). Laminar Pipe Flow with Injection and Suction Through a Porous Wall, *Transactions of the ASME*, (28), 719-724.

[10] **Dunlap, R., Willoughby, P.G., and Hermsen, R.W.** (1974). Flow Field in the Combustion Chamber of a Solid Rocket Propellant Motor, *AIAA Journal*, (12), 1440-1442.

[11] **Culick, F. E. C., and Magiawala, K.** (1979). Excitation of Acoustic Modes in a Chamber by Vortex Shedding, *Journal of Sound and Vibration*, *84*, (2), 455-457.

[12] **Dunlap, R., and Brown, R. S.** (1981). Exploratory Experiments on Acoustic Oscillations Driven by Periodic Vortex Shedding, *AIAA Journal*, *19*, (3), 408-409.

[13] **Nomoto, H. and Culick, F. E. C.** (1982). An Experimental Investigation of Pure Tone Generation by Vortex Shedding in a Duct, *Journal of Sound and Vibration*, *84*, (2), 247-252.

[14] **Isaacson, L. K., and Marshall, A. G.** (1982). Acoustic Oscillations in Internal Cavity Flows: Nonlinear Resonant Interactions, *AIAA Journal*, *20*, (1), 152-154.

[15] **Dunlap, R., Blackner, A.M., Waugh, R. C., Brown R. S., and Willoughby, P. G.** (1990). Internal Flow Field Studies in a Simulated Cylindrical Port Rocket Chamber, *Journal of Propulsion and Power*, *6*, (6), 690-704.

[16] **Traineau, J. C., Hervat, P., and Kuentzmann, P.** (1986). Cold-Flow Simulation of a Two-Dimensional Nozzleless Solid Rocket Motor, *AIAA Paper*, 86-1447.

[17] **Balakrishnan, G., Linan, A., and Williams, F. A.** (1992). Rotational Inviscid Flow in Laterally Burning Solid-Propellant Rocket Motors, *Journal of Propulsion and Power*, *8*, (6), 1167–1176.

[18] **Hegab, A. M., Sait, H. H., Hussain, A., and Said, A. S.** (2014). Numerical Modeling for the Combustion of Simulated Solid Rocket Motor Propellant, *Computers & Fluids*, *89*, 29-37.

[19] **Vuillot, F., Basset, T., Dupays, J., Daniel, E., and Lupoglazoff, N.** (1997) 2D Navier-Stokes Stability Computations for Solid Rocket Motors: Rotational, Combustion and Two-Phase Flow Effects, *AIAA*, *3326*, 1-11.

[20] **Lupoglazoff, N., and Vuillot, F.** (1992). Numerical Simulation of Vortex Shedding Phenomenon in 2D Test Case Solid Rocket Motors, *AIAA*, *0776*, 1-9.

[21] **Kirkkopru, K., Kassoy, D.R., and Zhao, Q.** (1996). Unsteady Vorticity Generation and Evolution in a Model of a Solid Rocket Motor, *Journal of Propulsion and Power*, *12*, (4), 646-654.

[22] **Staab, P.L., Zhao, Q., Kassoy, D.R., and Kirkkopru, K.** (2000). Acoustically Generated Vorticity in an Internal Flow, *Journal of Fluid Mechanics*, *413*, 247-285.

[23] **Alavilli, P., Buckmaster, J., Jackson, T. L., and Short, M.** (2000). Ignition-Transient Modeling for Solid Propellant Rocket Motors, *AIAA*, *3567*, 1-9.

[24] **Lupoglazoff, N., and Vuillot, F.** (1991). Two-Dimensional Numerical Simulation of the Stability of a Solid Propellant Rocket Motor, *AIAA Paper 91-0205*, AIAA 29th Aerospace Sciences Meeting, Reno, Nevada, USA.

[25] **Staab, P.L., Zhao, Q., Kassoy, D.R., and Kirkkopru, K.** (1999). Co-existing Acoustic-Rotational Flow in a Cylinder with Axisymmetric Sidewall Mass Addition, *Physics of Fluids*, (11), 2935-2951.

[26] **Menon, S., and Jou, W. H.** (1990). Numerical Simulations of Oscillatory Cold Flows in an Axisymmetric Ramjet Combustor, *Journal of Propulsion and Power*, *6*, (5), 525-534.

[27] **Apte, S., and Yang, V.** (2001). Unsteady Flow Evolution in a Porous Chamber with Surface Mass Injection, *AIAA Journal*, (39), 1577-1586.

[28] **Kirkkopru, K., Kassoy, D.R., Zhao, Q., Staab, P.L.** (2002). Acoustically Generated Unsteady Vorticity Field in a Long Narrow Cylinder with Sidewall Injection, *Journal of Engineering Mathematics*, (42), 65-90.

[29] **Apte, S., and Yang, V.** (2002). Unsteady Flow Evolution in a Porous Chamber with Surface Mass Injection, II: Acoustic Excitation, *AIAA Journal*, (40), 244-253.

[30] **Apte, S., and Yang, V.** (2003). A Large-Eddy Simulation Study of Transition and Flow Instability in a Porous-Walled Chamber with Mass Injection, *Journal of Fluid Mechanics*, *477*, 215-225.

[31] **Kourta, A**, (2004). Instability of Channel Flow with Fluid Injection and Parietal Vortex Shedding, *Computers & Fluids*, (33), 155-178.

[32] **Liou, T.M., and Lien, W.Y.** (1995). Numerical Simulations of Injection Driven Flows in a Two-Dimensional Nozzless Solid Rocket Motor, *Journal of Propulsion and Power*, (11), 600-606.

[33] **Ciucci, A., Iaccarino, G., Moser, R., Najjar, F., and Burbin, F.** (1998). Simulation of Rocket Motor Internal Flows with Turbulent Mass Injection, *Proceedings Summer Program Center for Turbulence Research*, Stanford University, 245-266.

[34] **Taylor, G.** (1996). Fluid Flow in Regions Bounded by Porous Surfaces, *Journal of Computational Physics*, 234, 456-476.

[35] **Vuillot, F.** (1991). Numerical Computation of Acoustic Boundary Layers in Large Propellant Space Boosters, *AIAA Paper 91-0206*, Reno, January.

[36] **Anderson, H. D.** (1970). *A Time Dependent Analysis for Vibrational and Chemical Non-Equilibrium Nozzle Flows*, *8*, 3, 545-550.

[37] **Apte, S. and Yang, V.** (2002). Unsteady Flow Evolution and Combustion Dynamics of Homogenous Solid Propellant in a Rocket Motor, *Combustion and Flame*, *131* (1-2), 110-131.

[38] **El-Askary, W. A., Wilson, S. A., and Hegab, A.** (2011). Simulation of Reactive Fluid Flow in a Solid Rocket Motor Combustion-Chamber with/without Nozzle, *CMES*, *76*, (4), 235-266

[39] **Chu, W. W., Yang, V., and Majdalani, J.** (2003). Premixed Flame Response to Acoustic Waves in a Porous-Walled Chamber with Surface Mass Injection, *Combustion and Flame*, 133, 359-370.

[40] **Yumusak, M.** (2000). *Non-Reacting and Reacting Flow Analysis in Propulsion Systems*, (Ph.D. Thesis), Middle East Technical University, Ankara.

[41] **Barth, T. J., and Steger, J. L.** (1984). An Efficient Approximate Factorization Implicit Scheme for the Equations of Gas Dynamics, *NASA Technical Memorandum 85957*.

[42] **Bohn, D., Schönenborn, H., and Wilhemi, H.** (1995). Numerical Simulation of Supersonic, Chemically Reacting Flow Using an Implicit Finite Volume Method, *Journal of Thermophysics and Heat Transfer*, *11*, (1), 45-51.

[43] **Krispin, J., and Anderson, J.D.** (1988). Accelerating the Computation of Steady State Solutions for Non-Equilibrium Chemically Reacting Flow Fields, *AIAA Paper* 85-0513, Reno, NV.

[44] **Candler, G. V.** (1998). *The Computation of Weakly Ionized Hypersonic Flows In Thermo-Chemical Non-Equilibrium*. (Ph.D. Thesis), Stanford University, Stanford, CA.

[45] **Gökçen, T.** (1989). *Computation of Hypersonic Low-Density Flows with Thermochemical Non-Equilibrium*. (Ph.D. Thesis), Stanford University, Stanford, CA.

[46] **George, E**. (1986). *Gas Dynamics: Theory and Applications*, AIAA Education Series.

[47] **McAmis, R., and Lankford, D**, (1991). Application of Chemically Reacting Navier-Stokes Code for Predicting Nozzle Performance of a High Area Ratio Liquid-Propellant Rocket Engine, *AIAA Paper 91-0307*.

[48] **Vos, J. B., and Bergman C. M.** (1991). Chemical Equilibrium and Non-Equilibrium Inviscid Flow Simulations Using and Explicit Scheme, *Computer Physics Communications*, *65*, (1-3), 289-298.

[49] **Yee, H.C., and Shinn, J.L.** (1989). Semi-Implicit and Fully Implicit Shock-Capturing Methods for Nonequilibrium Flows, *AIAA Journal*, *27*, (3), 299-307.

[50] **Sutton, G. P.** (1992). *Rocket Propulsion Elements*, Wiley, New York, Ch. 11, pp. 417-437.

[51] **Uygun, M., and Kirkkopru, K.** (2009). Numerical Simulation of Unsteady Flows in Solid Rocket Motors with Dual Time Stepping, *ITU Dergisi/d: Muhendislik*, *8*, (2), 41-52.

[52] **Terzic, J., Zecevic, B., Serdarevic-Kadic, S., and Catovic, A.** (2012). Numerical Simulation of Internal Ballistics Parameters of Solid Propellant Rocket Motors, *15th Seminar "New Trends in Research of Energetic Materials"*, University of Pardubice, Czech Republic, Part II, 881-892, ISBN 978-89-7395-480-2.

[53] **Tola, C.** (2017). *Çok Disiplinli Yaklaşımla Katı Yakıtlı Roket Motoru Yapısal Dayanım ve İç Balistik Performans Optimizasyonu*, (Ph.D. Thesis), Istanbul Technical University, Istanbul.

[54] **Li, Q., He, G., Liu, P., and Li, J.** (2014). Coupled Simulation of Fluid Flow and Propellant Burning Surface Regression in a Solid Rocket Motor, *Computers and Fluids*, *93*, 146-152.

[55] **Greatrix, D.** (2015). Numerical Evaluation of the Use of Aluminum Particles for Enhancing Solid Rocket Motor Combustion Stability, *Energies*, *8*, 1195-1215.

[56] **Montesano, J., Behdinan, K., Greatrix, D. R., and Fawaz, Z.** (2008). Internal Chamber Modeling of a Solid Rocket Motor: Effects of Coupled Structural and Acoustic Oscillations on Combustion, *Journal of Sound and Vibration*, *311*, 20-38.

[57] **Wang, L., Wu, Z., Chi, H., Lui, C., Tao, H., and Wang, Q.** (2015). Numerical and Experimental Study on the Solid-Fuel Scramjet Combustor, *Journal of Propulsion and Power*, *31*, (2), 685-693.

[58] **Ward, J., Son, S. F., and Brewster, M. Q.** (1998). Role of Gas- and Condensed-Phase Kinetics in Burning Rate Control of Energetic Solids, *Combustion Theory and Modeling*, *2*, (3), 293–312.

[59] **Geckler, R. D.** (1993). *Selected Combustion Problems-AGARD*, Permagon Press, New York.

[60] **Gupta, G., Jawale, L., Mehilal, Bhattacharya, B.** (2015). Various Methods for the Determination of the Burning Rates of Solid Propellants-An Overview, *Central European Journal of Energetic Materials*, *12*, (3), 593-620.

[61] **Havlucu, M. O., and Kirkkopru, K.** (2016). Numerical Simulation of Flow in a Solid Rocket Motor: Combustion Coupled with Regressive Boundary, *Journal of Multidisciplinary Engineering Science and Technology*, *3*, (1), 3790-3798.

[62] **Williams, F.A.** (1985). *Combustion Theory: The Fundamental Theory of Chemically Reacting Flow Systems*, The Benjamin/Cummings Publishing Company, Inc.

[63] **ANSYS Fluent** (Version 15.0) [*Computer Software*], Canonsburg, PA, 2013.

[64] **Curtiss, C. F., and Hirschfelder, J.O.**, (1952). Integration of Stiff Equations, *Proceedings of the National Academy of Sciences of United States of America*. Wisconsin, Department of Chemistry, University of Wisconsin.

[65] **Kuentzmann, P.** (2004). *Introduction to Solid Rocket Propulsion*, *Internal Aerodynamics in Solid Rocket Propulsion*, RTO Educational Notes, EN-023.

[66] **Gossant, B.** (1993). *Solid Rocket Propulsion Technology*, Chapter 4, Solid Propellant Combustion and Internal Ballistics of Motors, Pergamon Press, Oxford, pp. 111-112

[67] **Microsoft Visual C++ 2010 Express** (Version 10.0.30319.1) [*Computer Software*], 2010.

[68] **Uygun, M.** (2007). *Numerical Simulation of Unsteady Flows in Solid Rocket Motors with Deforming Grids*, (Ph.D. Thesis), Istanbul Technical University, Istanbul.

[69] **Sankar, S. V., Jagoda, J. I., and Zinn, B. T.** (1990). Oscillatory Velocity Response of Premixed Flat Flames Stabilized in Axial Acoustic Fields, *Combustion and Flame*, 80, 371-384.

[70] **Majdalani, J., and Van Moorhem, W. K.** (2001). Laminar Cold-Flow Model for the Internal Gas Dynamics os a Slab Rocket Motor, *Aerosp. Sci. Technol.*, 5, 193-207.

[71] **Metglachi, M., and Keck, J. C**. (1982). Burning Velocities of Mixtures of Air with Methanol, Isooctane, and Indolene at High Pressure and Temperature, *Combustion and Flame*, 48, 191-210.

[72] **McBride, B. J., and Gordon, S.** (1994). CET93 and CETPC: *An Interim Updated Version of the NASA Lewis Computer Program for Calculating Complex Chemical Equilibria with Applications*, TM-4557, NASA, Technical Report.

[73] **Rogers, R. C., and Chinitz, W.** (1982). Using a Global Hydrogen-Air Combustion Model in Turbulent Reacting Flow Calculations, *AIAA Journal*, *21*, (4), 586-592.

APPENDICES

APPENDIX A: UDF DEFINE_GRID_MOTION
APPENDIX B: UDF DEFINE_EXECUTE_AT_END
APPENDIX C: DEFINE_PROFILE

APPENDIX A

```
DEFINE_GRID_MOTION(domain, dt, time, dtime)
{

	//Definitions of the Variables
	/*******************************************************************/
	face_t f;

	Node *node_p;
	Thread *tf = DT_THREAD (dt);
	real t = CURRENT_TIME;

	int n;



	SET_DEFORMING_THREAD_FLAG (THREAD_T0 (tf));

	//Position Update of node_p
	/*******************************************************************/
	begin_f_loop (f, tf)
	{
		f_node_loop (f, tf, n)
		{
			node_p = F_NODE (f, tf, n);

			if (NODE_POS_NEED_UPDATE (node_p))
			{
				NODE_POS_UPDATED (node_p);
				NODE_Y (node_p) = NODE_Y (node_p)-
(burningrate)*dtime;
			}

		}
	}
	end_f_loop (f, tf);
	/*******************************************************************/
		//fclose(fr);
}
```

APPENDIX B

```
DEFINE_EXECUTE_AT_END(burnratecalc)
{
real pressure=0.0;
Domain *d;
cell_t c;
face_t f;
Thread *t;
d = Get_Domain(1);
t= Lookup_Thread(d, 9);
begin_f_loop(f,t)
{
pressure+= C_P(c,t);
}
end_f_loop(f,t)

burningrate = a*(pow((pressure/1000000),n));
printf("Average Pressure: %f\n",pressure);

}
```

APPENDIX C

```
DEFINE_PROFILE(unsteady_mf_inlet, thread, position)
{
face_t f;
//real t = CURRENT_TIME;
begin_f_loop(f, thread)
{
F_PROFILE(f, thread, position) =densityofpropellant*burningrate;
}
end_f_loop(f, thread)
}
```

CURRICULUM VITAE

Name Surname **:** Mehmet Özer HAVLUCU

Place and Date of Birth **:** Elazığ 01/06/1976

E-Mail **:** ozerhavlucu@gmail.com

EDUCATION **:**

- **B.Sc.** **:** 1999, Istanbul Technical University, Mechanical Engineering Faculty, Mechanical Engineering Department
- **M.Sc.** **:** 2003, Boğaziçi University, Engineering Faculty, Mechanical Engineering Department

PROFESSIONAL EXPERIENCE AND REWARDS:

- 1999, First Prize in Machine Project 'Amfibic Vehicle' at ISTANBUL Technical University

PUBLICATIONS, PRESENTATIONS AND PATENTS ON THE THESIS:

- **Havlucu, M. O.**, and Kirkkopru, K. 2016. Numerical Simulation of Flow in a Solid Rocket Motor: Combustion Coupled with Regressive Boundary, Journal of Multidisciplinary Engineering Science and Technology, *3*, (1), 3790-3798.
- **Havlucu, M. O.**, and Kirkkopru, K. 2017. Numerical Simulation of Flow in a Solid Rocket Motor: Combustion Coupled Pressure Dependent Regressive Boundary, International Journal of Engineering Science Invention, *6*, (3), 54-65.